The Seasonal Variation of the Hydrologic Cycle as Simulated by a Global Model of the Atmosphere

SYUKURO MANABE AND J. LEITH HOLLOWAY, JR.

Geophysical Fluid Dynamics Laboratory/NOAA, Princeton University
Princeton, New Jersey 08540

A numerical model of the atmosphere with a seasonal variation of insolation and sea surface temperature is time integrated for over 3 simulation years on a finite difference grid network having a nearly uniform horizontal resolution of approximately 265 km. There are 11 levels in the model from 80 m to 31 km above the ground. The model has realistic continents with smoothed topography. In addition to wind, temperature, pressure, and water vapor, the model simulates rainfall, snowfall, and evaporation at the surface. The runoff rate and the rates of change of soil moisture and snow depth are determined by a budget of liquid water, snow, and heat at the ground surface. The simulated precipitation and other hydrologic quantities are compared with those derived from observed data. In addition, the correspondence between the distribution of precipitation rate and those of other relevant quantities, such as sea level pressure and kinetic energy of transient disturbances, is examined. To obtain an overall impression of the climate simulation, a map of Köppen climate types, which is obtained from simulated temperatures and precipitation rates throughout the year, is compared with a similar map based upon observed climatic data. It is shown that the model locates the major arid regions of the earth, such as the Sahara Desert in northern Africa and the deserts of central Asia and Australia. Furthermore, the tropical rain belt and its seasonal movement are well reproduced. The model approximately simulates the changeover from dry winter to wet summer conditions in southern Asia and the seasonal reversal of the monsoon wind system over Asia. The wet zone in middle and high latitudes, such as in Canada, Europe, and western Siberia, is also simulated by the model. Examination of the distribution of runoff over continents of the model reveals that the watersheds of many important rivers of the world are correctly positioned in the simulation. In general, the quality of the simulation tends to deteriorate in the neighborhood of major mountain ranges. Furthermore, the rate of precipitation and that of runoff over continental regions in the model tropics is much larger than estimates of the actual rates of these quantities. Nevertheless, this study demonstrates that the model is capable of reproducing many of the basic features of the seasonal variation of hydrology and climate on a global scale.

INTRODUCTION

This study presents a comprehensive description of the seasonal variation of the hydrologic cycle obtained from a mathematical model of the atmosphere. The ultimate goal of studies of this kind is to construct a sufficiently realistic model of climate so that one can perform various controlled numerical experiments to investigate how climate is maintained or why climate changes.

Since an important factor controlling climate and the atmospheric circulation is the hydrologic cycle, it is indispensable to incorporate the hydrologic processes into any mathematical model of the atmosphere used for the simulation of climate. *Manabe et al.* [1965] constructed a model which included a system of primitive equations of motion and highly idealized processes representing precipitation and evaporation. Their model has a flat and uniformly wet surface without any heat capacity. It was shown that their model can reproduce some of the zonal mean properties of precipitation, such as the tropical rain belt, the dry belt in the subtropics, and the rain belt in middle latitudes. *Leith* [1965] made a model with actual distributions of continents and oceans in which observed distributions of sea surface temperature are prescribed as a lower-boundary condition. His model reproduced some of the features of the hydrologic cycle, but the details of his results are not available.

Washington and Kasahara [1970] constructed a two-level general circulation model with realistic orography. Assuming the distribution of insolation and sea surface temperature in January, they were able to reproduce some of the zonal mean features of the hydrologic cycle. This study was repeated by *Kasahara and Washington* [1971] with a six-level general circulation model which reproduces some of the geographical distributions of precipitation.

The various models of climate which are mentioned above do not take into consideration the variation of soil moisture and snow cover. Instead, the soil is assumed to be either completely wet or completely dry throughout the time integration of the model. Therefore these models fail to simulate some of the important features of the geographical distribution of the climate which are strongly controlled by soil moisture and snow cover. To eliminate this difficulty, *Manabe* [1969] proposed a highly idealized scheme for predicting soil moisture and snow cover for incorporation into a general circulation model. Although his model has a limited computational domain and idealized geography, it reproduces some of the essential characteristics of the geographical distributions of hydrologic quantities. Encouraged by these results, *Manabe and Holloway* [1970] constructed a global model with the hydrologic processes mentioned above and successfully simulated many basic features of the global distributions of precipitation, soil moisture, and runoff, during January [*Holloway and Manabe*, 1971]. Similar processes of the hydrology at the ground surface have recently been incorporated into the model of Washington and Kasahara [*Washington*, 1971], although the details of the geographical distributions of hydrologic quantities have not been published.

This study is a natural extension of the work of Holloway and Manabe mentioned above. We describe how the hydrologic cycle of the model responds to seasonal variations of insolation and sea surface temperature. In addition, details of the model climate are compared with the actual climate.

Preliminary results from this study were presented at the

Climate Symposium held at Leningrad in 1971 [*Manabe et al.*, 1971] and at the Summer Computer Simulation Conference held at Houston, Texas, July 9–11, 1974 [*Holloway and Manabe*, 1974].

Some results from this model simulation, related to the general circulation and climate of the tropics, have already been published in a companion paper by *Manabe et al.* [1974].

DESCRIPTION OF THE MODEL

The numerical model used in this study is very similar to the one described by *Holloway and Manabe* [1971] with the exception that the solar radiation, concentrations of atmospheric ozone, and sea surface temperatures prescribed undergo a seasonal variation. Therefore only a brief description of the model is given here.

The model solves the primitive equations of motion in a spherical coordinate system. The numerical problems introduced by mountains are reduced by using the sigma coordinate system in which pressure normalized by surface pressure is the vertical coordinate [*Phillips*, 1957]. To simulate the effects of subgrid scale mixing, the nonlinear viscosity of *Smagorinsky* [1963] is included in the model. The finite difference forms of the dynamical equations are similar to those proposed by *Kurihara and Holloway* [1967]. The global grid system is chosen such that the horizontal grid size of approximately 265 km is as uniform as possible. The 11 finite difference levels are selected so that the model can simulate the structures of both the stratosphere and the planetary boundary layer. (See Table 1 of *Manabe et al.* [1974] for details.)

A global map of the smoothed continental topography used by the model appears in Figure 1. The method used for deriving these mountain heights and the degree of smoothing applied are the same as used by *Holloway and Manabe* [1971] for their high-resolution (N48) model.

The scheme for computing radiative heating and cooling is described by *Manabe and Strickler* [1964] and *Manabe and Wetherald* [1967]. The solar radiation at the top of the atmosphere is a function of both latitude and season, but its diurnal variation is eliminated for simplicity. The seasonal variation of insolation is controlled by changes in both solar declination and distance, which are functions of the date. An annual mean observed distribution of clouds, which varies with latitude and height but not with longitude, is used in the computation of radiative transfer. In addition, the effects of water vapor, carbon dioxide, and ozone are taken into consideration. The distribution of water vapor is determined by the prognostic equations of the model. An observed distribution of ozone [*Hering and Borden*, 1965], which varies with season, latitude, and height, is specified for the radiative transfer computation. The mixing ratio of carbon dioxide by weight is assumed to have a constant value of 0.456×10^{-3} everywhere.

The surface temperature over land is determined by the boundary condition that no heat is stored in the ground, i.e., net fluxes of solar and terrestrial radiation and turbulent fluxes of sensible and latent heat locally add to zero. Over the oceanic part of the model the seasonal variation of surface temperature is prescribed. It is determined by harmonic curve fitting over four observed distributions of monthly mean sea surface temperatures, i.e., those for February, May, August, and November. Data from the *World Atlas of Sea Surface Temperatures*, which has been recently revised by the *U.S. Navy Hydrographic Office* [1964], are used for this purpose. The surface temperature of sea ice is computed in a manner similar to the computation of land surface temperature, except that heat conduction through ice is taken into consideration. On the basis of various oceanographic data we assumed that the Arctic Ocean is covered by a uniform layer of sea ice with a thickness of 2 m. (For example, *Neumann and Pierson* [1966] state that the inner 70% of the Arctic Ocean is covered by pack ice ranging from 2 to 3.5 m thick.)

The prognostic system of water vapor mainly consists of the contributions by the three-dimensional advection of water vapor, evaporation from the earth's surface, vertical mixing of water vapor in the planetary boundary layer, nonconvective condensation, and a so-called 'moist convective adjustment.' For a more specific description of moist convective adjustment, see *Manabe et al.* [1965].

Fig. 1. Global map of smoothed land topography and shorelines used by the model. Areas having elevations between 1 and 3 km are shaded with dots and greater than 3 km, with diagonal lines.

The schemes for computing the hydrology of the ground surface are similar to those described by *Manabe* [1969]. The rates of the change of soil moisture and snow depth are determined by the budget of water, snow, and heat at the ground surface. Since the simulation of the hydrologic process is emphasized in this study, we decided to describe these schemes in some detail.

The maximum amount of water that can be stored in the ground, called the field capacity of the soil, depends upon a number of characteristics of the ground surface and thus varies considerably throughout the world. For simplicity we have set the field capacity of the soil to 15 cm over all land areas. Most of the time the actual soil moisture falls short of the field capacity of the soil at a given point. In the model a budget of soil moisture is kept at each land grid point. Changes in soil moisture are computed as the residual of contributions from processes that increase soil moisture (i.e., rainfall and snowmelt) and those that decrease it (i.e., evaporation and runoff). Runoff is predicted at a grid point only if a computed change in soil moisture would result in a water depth exceeding the field capacity. Any moisture above 15 cm is thus computed as runoff at the grid point where this occurs. Runoff is assumed to flow directly to the sea via rivers without affecting the soil moisture at any other point.

The effect of soil moisture on evaporation is incorporated into the model by a simple scheme used by *Budyko* [1956]. When the soil does not contain a sufficient amount of water, the amount of evaporation is smaller than that from the sea or a perfectly wet surface. The sea case sets an upper limit for evaporation over a land surface under given surface wind and humidity conditions. If the soil moisture is greater than a certain critical percentage (75 in this study) of the maximum soil capacity, evaporation is assumed to equal the maximum rate. Otherwise, evaporation from land is computed to be linearly proportional to soil moisture up to this critical value. The rate of sublimation from the surface of snow or ice is computed under the assumption of water vapor saturation at the surface.

The rate of change of water equivalent depth of snow is computed as the residual of the rate of snowfall minus the sum of the snowmelt and sublimation rates. Precipitation, which is deduced from the prognostic system of water vapor mentioned earlier, is regarded as snowfall if the temperature at a height of 350 m is below freezing. The snowmelt rate is calculated from a surface heat budget under the assumptions that the temperature of the snow surface does not exceed the freezing point and that the conductivity of snow is zero.

The numerical time integration of the model is continued for a period of approximately 3.5 model years. The initial conditions for this integration were the mean state attained by the long-term integration of a global model in which January insolation and sea surface temperatures were the imposed boundary conditions. The first 1.5 model years were time integrated on a grid with approximately 530-km horizontal resolution. A high-resolution (approximately 265 km) grid is used for time integrating the final 2 model years. The results from the time integration of the final 1.75 model years are analyzed for this study.

TIME MEANS OF MODEL CLIMATIC VARIABLES

The annual means of various climatic variables presented in this paper are based on the last year of the time integration of the global seasonal model from August through July (model dates). Since seasonal variations are important characteristics of climate, annual means naturally do not fully describe the climates of most regions of the earth. For the sake of brevity in our discussions we shall present only winter and summer distributions of climatic variables in this paper. Winter in the northern hemisphere is assumed to include data from December, January, and February. Data from June, July, and August comprise the northern hemisphere summer averaging period. These seasons, of course, are reversed in the southern hemisphere.

Sea level pressure. Figure 2 presents the mean model-simulated sea level pressure for the period December through February compared with the observed mean pressure. The computed versus observed sea level pressure comparison for June through August is given in Figure 3. The observed mean pressures are based on data by *Crutcher and Meserve* [1970] in the northern hemisphere and by *Taljaard et al.* [1969] in the southern hemisphere. The surface pressure over land in the model results is reduced to sea level by

$$p_{SL} = p_* \left[\frac{T_{11}}{T_{11} + \gamma Z_*} \right]^{-g/R\gamma} \tag{1}$$

where p_{SL} is the sea level pressure; p_*, the surface pressure; T_{11}, the temperature of the lowest prognostic level; Z_*, the height of the land surface above sea level; γ, the lapse rate, assumed to be 6°K/km everywhere; and g, the acceleration of gravity.

The pressure distribution in the northern hemisphere in winter is well simulated by the global model. Both the Aleutian and Icelandic lows are correctly positioned by the model, but the intensity of the former is too great in the model simulation. The Asian anticyclone ('Siberian high') is also well placed by the model, but it is simulated to be too intense by about 10 mbar. The irregularity of the isobars at the southwestern side of this high-pressure area results from the large reduction to sea level from the great height of the Himalayan Plateau. The distribution of high pressure in the northern subtropics is also well simulated by the model at this season.

The mean pressure patterns in the model tropics during the December to February period coincide well with the observed values at this season. The large region of low pressure in the model over the tropical western Pacific Ocean corresponds to an area of maximum computed rainfall. The low centers simulated over South Africa and South America agree well with observation, and their positions reflect the southward shift of the tropical rain belt over continents, discussed in the following section.

As shown in Figure 2, the model simulates subtropical anticyclones of about the correct intensity off the three southern hemisphere continents in summer in excellent agreement with observation. However, the belt of low pressure just to the north of Antarctica is displaced northward and is too weakly developed in the model. For this reason, the strength of the southern hemisphere mid-latitude prevailing westerlies in the model is considerably below what is observed in the actual atmosphere. The reason for this major deficiency of the model has not been isolated, but it may be related to the failure of the model to handle the orographic effects of the Antarctic continent properly.

The distribution of mean computed sea level pressure for the period June through August, shown in Figure 3, exhibits marked contrast with that for the opposite season, but most of these changes also occur in the actual atmosphere. For example, the wintertime Asian anticyclone is replaced in summer by the extensive south Asian low, whose intensity is well simulated by the model except in the Tibetan Plateau region, where great height renders the model pressures reduced to sea

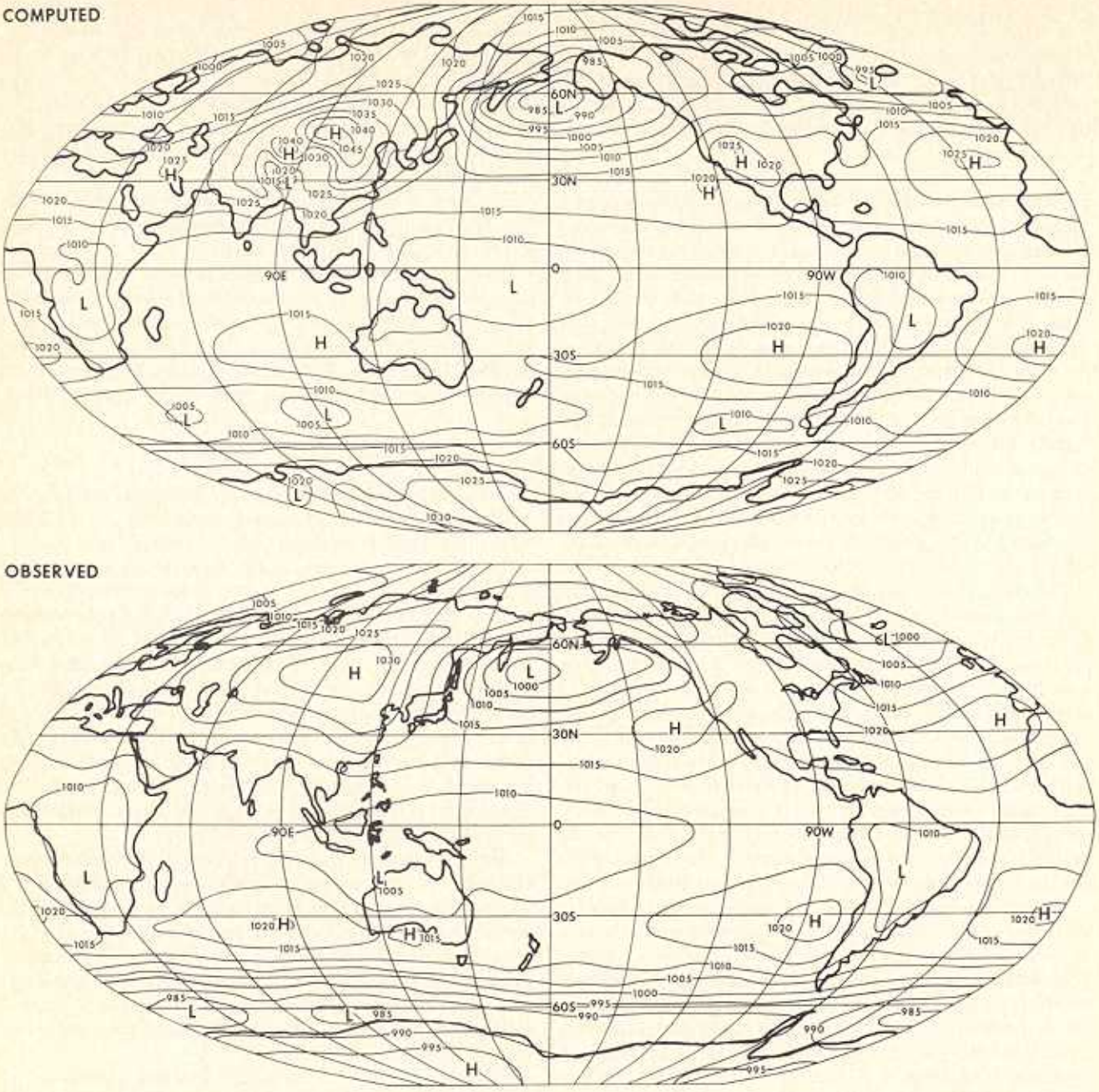

Fig. 2. Mean global sea level pressure for December, January, and February computed by the model (top) and observed in the actual atmosphere (bottom) as derived from data by *Crutcher and Meserve* [1970] and *Taljaard et al.* [1969].

level unreliable. This south Asian low plays an important role in maintaining the circulation of the Asian summer monsoon. For a further discussion of this subject, see *Hahn and Manabe* [1975].

The model simulates a belt of low pressure in the tropics in agreement with the observed mean pressure for the period June through August. The eastward-extending trough in the tropical portion of the western Pacific, both in the model results and in nature, corresponds to the spawning area of summer typhoons. In the model, however, tropical cyclones form too often, and their frequent passage northward along the Chinese coast creates a mean surface pressure in this region which is below the observed value [*Manabe et al.*, 1974].

In the subtropics of the model an anticyclone develops off the west coast of California in agreement with the features of the observed distribution. It does not, however, extend far enough toward the west because of the excessive development of low pressure in the western Pacific, mentioned above. The Atlantic high is not obvious in the model results because it has combined with the high-pressure center over the north polar region. In the southern hemisphere a belt of high pressure invades Australia and the southern tip of Africa and crosses South America around 30°S, in agreement with the observed pressure distribution.

The surface pressure in this model is too high over both poles. The excessive pressure in the model Arctic appears to be caused by a systematic error involved in the finite difference computation on the Kurihara-type irregular grid system used for time integrating this model. A model very similar to this one was time integrated on a regular latitude-longitude grid by

Holloway et al. [1973], and the tendency for the development of excessive north polar pressures was corrected for the most part. However, the high pressures over and around the steep Antarctic continent were not reduced satisfactorily.

Transient eddy kinetic energy. One of the important factors which controls climate is the activity of large-scale disturbances in the atmosphere. Figure 4 shows the global distributions of the transient component of eddy kinetic energy at the 850-mbar level of the model atmosphere during the months of January and July. The transient eddy kinetic energy (TKE) is defined by

$$\mathrm{TKE} = \tfrac{1}{2}(\langle u'^2 \rangle + \langle v'^2 \rangle) \qquad (2)$$

where u and v denote the zonal and meridional components of the wind, respectively. The angle brackets and prime indicate the time mean (1 month) operator and the deviation from the time mean, respectively.

In the middle latitudes of the northern hemisphere the model maintains areas of relatively large eddy kinetic energy, such as in the north Pacific and north Atlantic oceans in January. As is known, the great contrast in surface temperature between continents and oceans enhances air mass modification off the east coasts of the continents and promotes the development of cyclones there. The longitudinal variation of TKE is less pronounced in middle latitudes of the southern hemisphere, where the continents are smaller than those in the northern hemisphere. One can identify a zonal belt of large TKE in the latitude belt ranging from 40° to 50°S, particularly during winter.

In low latitudes the model maintains areas of large TKE in

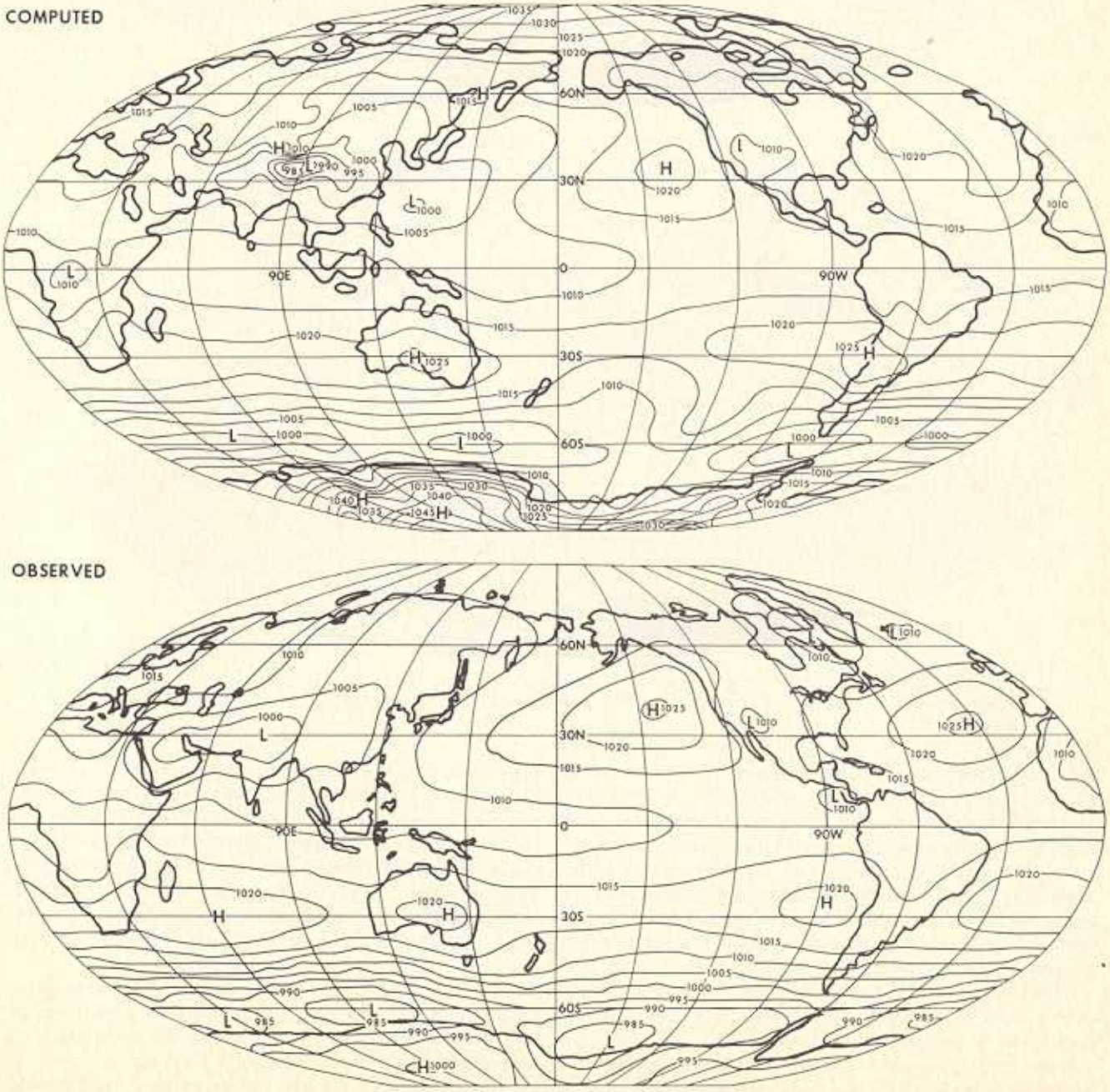

Fig. 3. Same as Figure 2 but for June, July, and August.

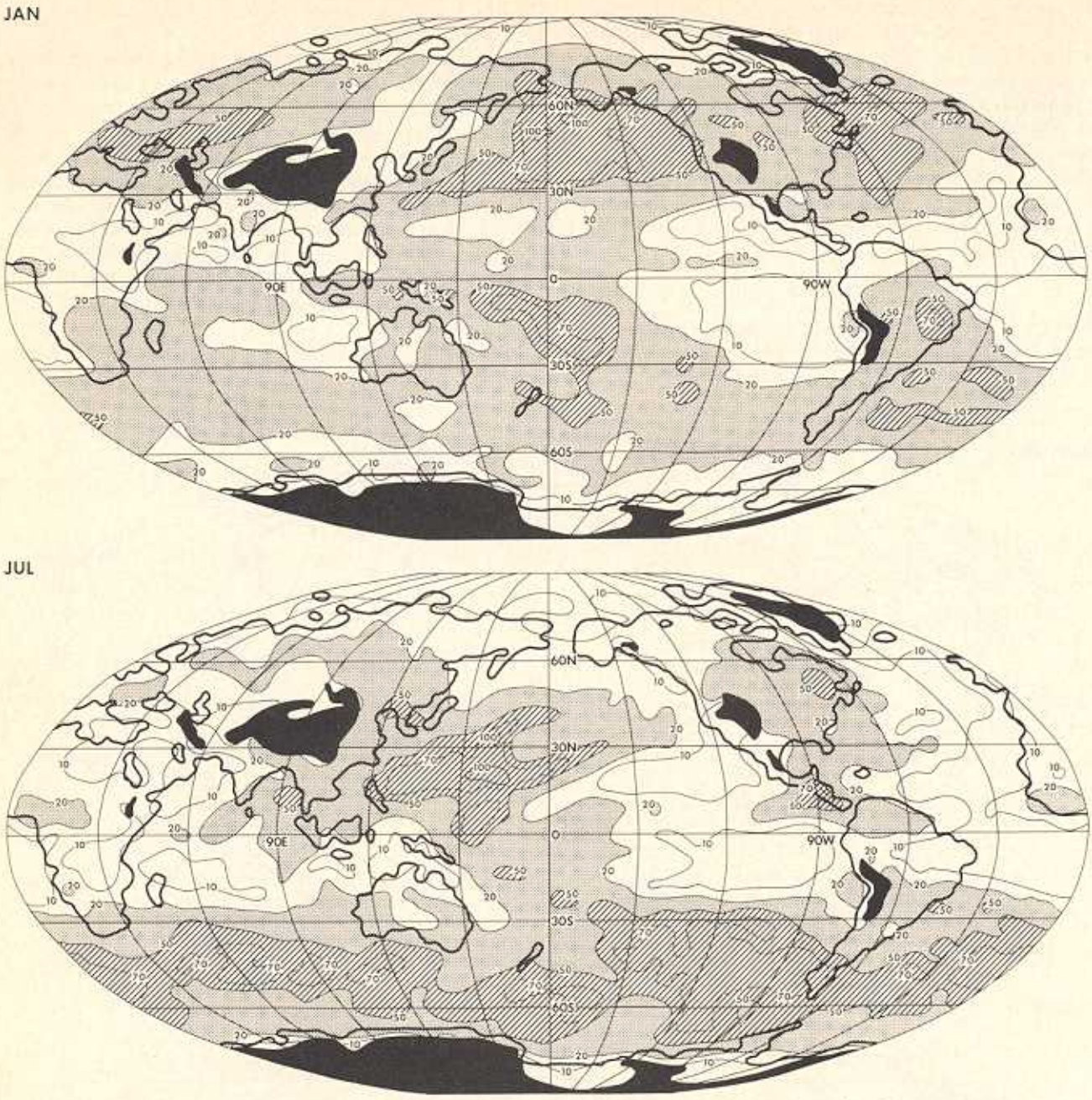

Fig. 4. Global distributions of transient eddy kinetic energy per gram at 850 mbar in units of square meters per square second for January (top) and July (bottom). Values greater than 25 are shaded and greater than 50, darkly shaded.

the summer hemisphere. In July, TKE is relatively large in the Philippine Sea, Central America, and in the Bay of Bengal. In January it is particularly large to the east of New Guinea and Australia. In a companion paper, which presents the general circulation in the tropical part of the model atmosphere, *Manabe et al.* [1974] pointed out that the disturbances in the model tropics are maintained against dissipation by the heat of condensation and tend to develop in areas of relatively warm sea surface temperatures.

In general, the areas of relatively large TKE approximately correspond with areas of high precipitation rate. This subject is discussed in the following section.

Mean vertical motion. Figure 5 shows the global distributions of the 3-month mean vertical p velocity at the 835-mbar level of the model atmosphere during two seasons of the year. According to the comparison between this figure and Figures 2 and 3, the areas of mean downward motion (positive vertical p velocity) correspond well with those of relatively high sea level pressure. For example, general downward motion occupies areas of subtropical anticyclones. On the other hand, upward motion prevails in areas of surface cyclones, such as in the Aleutian low. As expected, areas of mean downward motion also tend to coincide with those of meager precipitation rate discussed in the following section.

Surface air temperature. In Figure 6 the observed distribution of mean surface ambient air temperature over the entire earth during January is compared with the mean values of temperature at the lowest prognostic level computed by the time integration during model January. Figure 7 presents the same comparison for observed and computed July

temperature distributions. The observed temperatures in the northern hemisphere are derived from data by *Crutcher and Meserve* [1970] and in the southern hemisphere by *Taljaard et al.* [1969].

Understandably, the computed surface air temperatures over the oceans ought to agree well with the observed values during both January and July because the model used observed sea surface temperatures as a lower-boundary condition. In middle latitudes of both hemispheres this does appear to be true. However, in the tropics the simulated surface air temperatures are up to 3° too cool. Some of this discrepancy may result from inaccurate formulations of the convective process in the Ekman boundary layer and particularly the mixing in the constant flux layer. Furthermore, the lowest prognostic level is much higher than the so-called ship deck level, where ambient temperature is usually observed over oceans.

In general, the winter temperatures in the Eurasian continent and North America are well simulated by the model. For example, the tight packing of isotherms along the east coast of Asia and the northwest coast of North America in the model agrees with observation. Over the northern part of the Eurasian continent, surface temperature decreases progressively from Europe to eastern Siberia, where it is at a minimum, in agreement with a feature of the actual atmosphere. The very low temperatures in eastern Siberia result not only from radiative cooling but also from the thermal advection by cold northerlies which prevail in the area between the semipermanent Aleutian low and the Siberian high. On the other hand, western Siberia and Europe are kept warmer in winter by

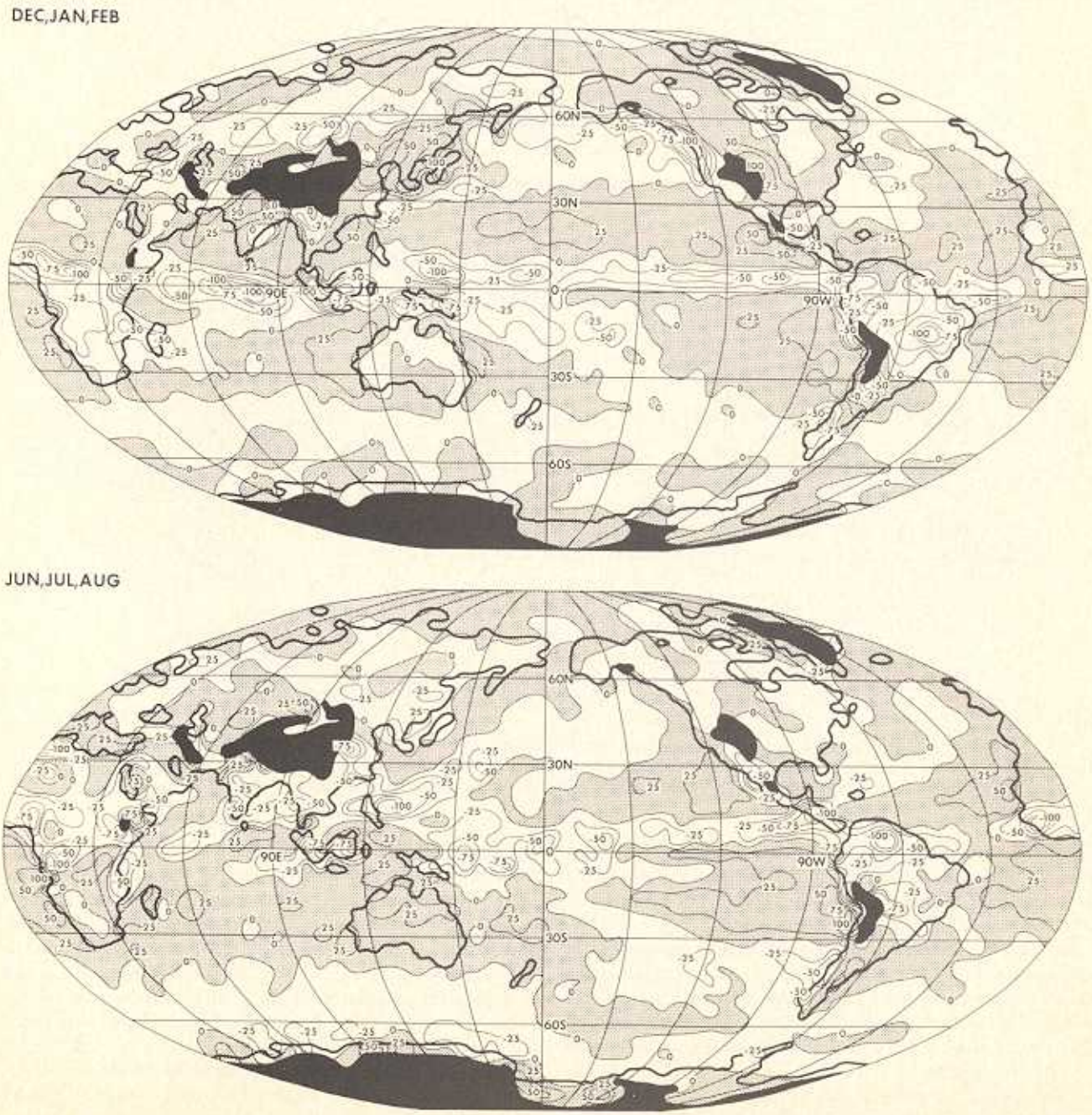

Fig. 5. Global distributions of vertical p velocity at 850 mbar in units of millibars per day for December, January, and February (top) and June, July, and August (bottom). Areas of positive values (downward motion) are shaded.

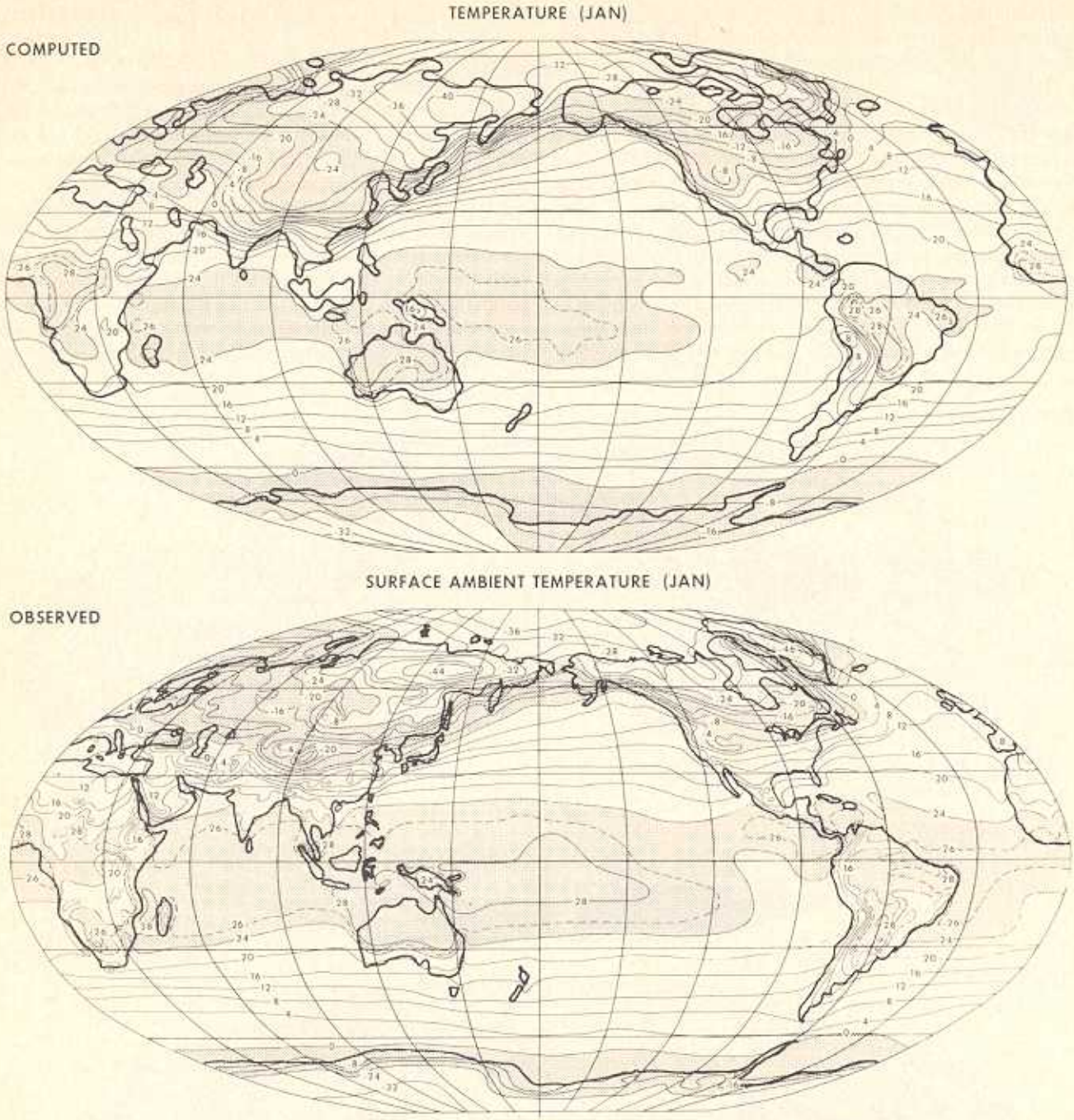

Fig. 6. Global distribution of mean temperatures simulated in the model for the lowest prognostic level (top) compared with that of the mean observed surface ambient temperature (bottom) for January in degrees Celsius (derived from data by *Crutcher and Meserve* [1970] and *Taljaard et al.* [1969]). Areas having temperatures above 24°C or between 0 and −24°C are shaded.

warm air advection behind the Asian anticyclone. Northeast Siberian temperatures are lower than those over the Arctic Ocean ice pack to the north because they are not tempered by heat conduction from an underlying ocean.

Summertime temperatures are higher in arid regions than in wetter areas at the same latitude and altitude. For example, the deserts northeast of the Caspian and Aral seas are warmer than European countries 2000–3000 km due west. The high air temperatures over dry territories are attributed to intense insolation coupled with low evaporation and weak moist convective activity. In order to satisfy the condition of surface heat balance the ground temperature must be high so that the resulting large heat loss from the upward fluxes of sensible heat and radiation can compensate for the small contribution from evaporational cooling. In general, the model reproduces these warm temperatures over arid regions in summer not only in the central Asian deserts and steppes but also in the Sahara and Australian deserts and many other dry areas around the world. In some areas, such as northern Africa, the model summer air temperatures, however, do not attain quite as high values as in nature. On the other hand, simulated surface air temperatures in July are too high in south central United States and in China, but this is probably due to the drier-than-actual climate created in these areas by the model, as is to be discussed in the following sections.

Finally, the model correctly simulates the strong

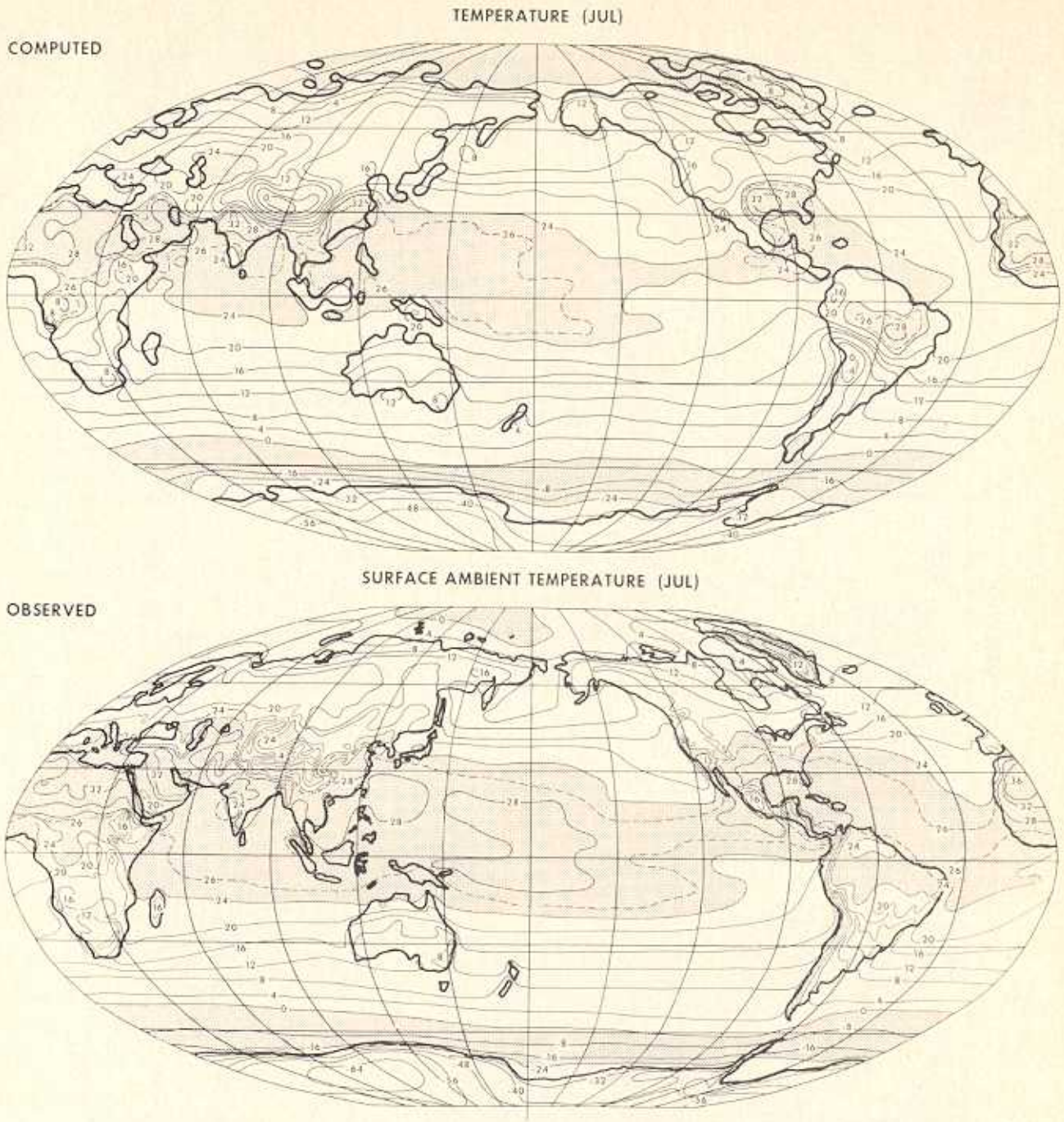

Fig. 7. Same as Figure 6 but for July.

temperature gradient perpendicular to the periphery of the Antarctic continent. This gradient is especially strong in July during the southern hemisphere winter. This large temperature gradient results mainly from the steep slope of the Antarctic mountains as well as the high surface albedo of the continent. In fact, the packing of the isotherms is so great that south of the 0°C isotherm, around 60°S latitude, isotherms for negative temperatures are drawn for only every 8°C in Figures 6 and 7. The lowest Antarctic temperatures attained in the model are somewhat higher than the observed values.

Meridional circulation. The annual mean state of the meridional circulation of the model atmosphere and its seasonal variation are illustrated in Figure 8. It shows the stream function of the mean meridional circulation in both the model and the actual atmosphere averaged over the entire year and over January and July. The annual mean stream function diagram based on the model simulation shows two moderate-strength Hadley cells nearly symmetrically located on each side of the equator. These cells are centered at about 11°N and 11°S, in very good agreement with the locations derived by *Oort and Rasmusson* [1970] from observed data. The weak Ferrel cells in the model's middle latitudes occur in the annual mean meridional circulation graph at 46°N and 41°S. The position and strength of the computed northern hemisphere reverse circulation cell agree closely with the actual atmosphere. The observed distribution does not extend far enough south to verify the simulation of the southern hemisphere Ferrel cell.

In general, the centers of both the Hadley and Ferrel cells of this model are located significantly lower in altitude than those

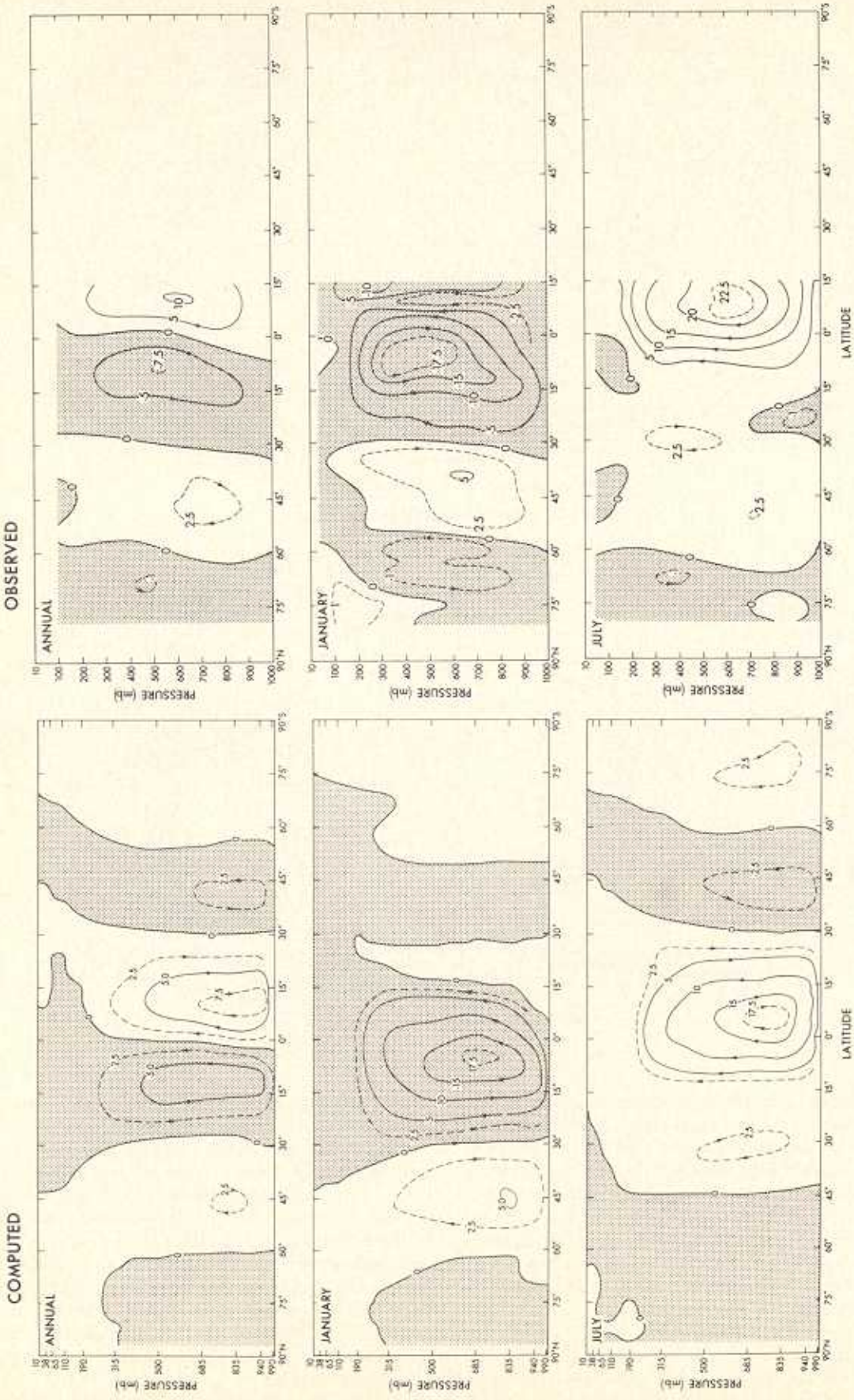

Fig. 8. Time mean stream function (10^{12} g s^{-1}) of the meridional circulation for the entire year (top), for January (middle), and for July (bottom); computed (left); observed (right) [*Oort and Rasmusson, 1971*].

in the actual atmosphere determined by Oort and Rasmusson. *Manabe et al.* [1974] speculated that this discrepancy results from the assumption of no vertical mixing of momentum above the planetary boundary layer of the model. Further numerical experimentation is required for evaluation of this speculation.

The simulated meridional flow for January exhibits a huge northern Hadley cell having an intensity of 18×10^{10} g s^{-1} and centered at about 5°N. This is in excellent agreement with the location and strength of this cell inferred from observed data. On the other hand, the southern Hadley cell at about 20°S is practically nonexistent. In July it is the southern Hadley cell which predominates in the model simulation, as shown in Figure 8. This large cell straddles the equator with an intensity of about 18×10^{10} g s^{-1}. For further discussion of the seasonal variation of the tropical Hadley cells, see *Manabe et al.* [1974].

Baroclinically unstable waves drive the reverse or Ferrel meridional circulation [*Phillips*, 1954]. Therefore it is understandable that the simulated Ferrel cell is at its maximum intensity in the winter hemisphere, when atmospheric eddy kinetic energy in middle latitudes is greatest. The strengths of both the simulated and the actual northern Ferrel cells are about 5×10^{10} g s^{-1} in winter and approximately half this value in summer. The locations of these Ferrel cells are somewhat indefinite, especially in summer, but in general the model positions are not at all inconsistent with those derived for the actual atmosphere.

Water vapor. The latitude-height distributions of zonal-mean relative humidity in the model are shown in Figure 9 for the periods December through February and June through August. At all latitudes the surface relative humidity is too high. (For the observed distribution of zonal-mean relative humidity, see, for example, Figure 7.3 of *Manabe et al.* [1965].) This bias has not been explained, but it may be partly attributed to deficiencies in the model's moist convective adjustment or vertical diffusion formulations. (Note that in this model the critical relative humidity for the onset of moist convection is assumed to be 100%, which seems to be too high.)

On the other hand, the model's stratosphere is very dry at all seasons except at high latitudes in the winter hemisphere. This is consistent with moisture conditions thought to exist in the actual stratosphere, although humidity measurements are very inaccurate at these heights. High relative humidities at the extremely cold temperatures of the winter polar stratosphere probably exist in the real atmosphere as evidenced by the occasional development of mother-of-pearl clouds at high latitudes in winter.

The latitude-height distribution of the zonal-mean relative humidity, shown in Figure 9, is strongly controlled by the meridional circulation discussed in the previous subsection. The rising air in the Hadley cells creates a column of relatively high humidity above the tropical rain belt, which in the mean is near the equator in the December–February period and around 10°N in the June–August period. This rising moisture

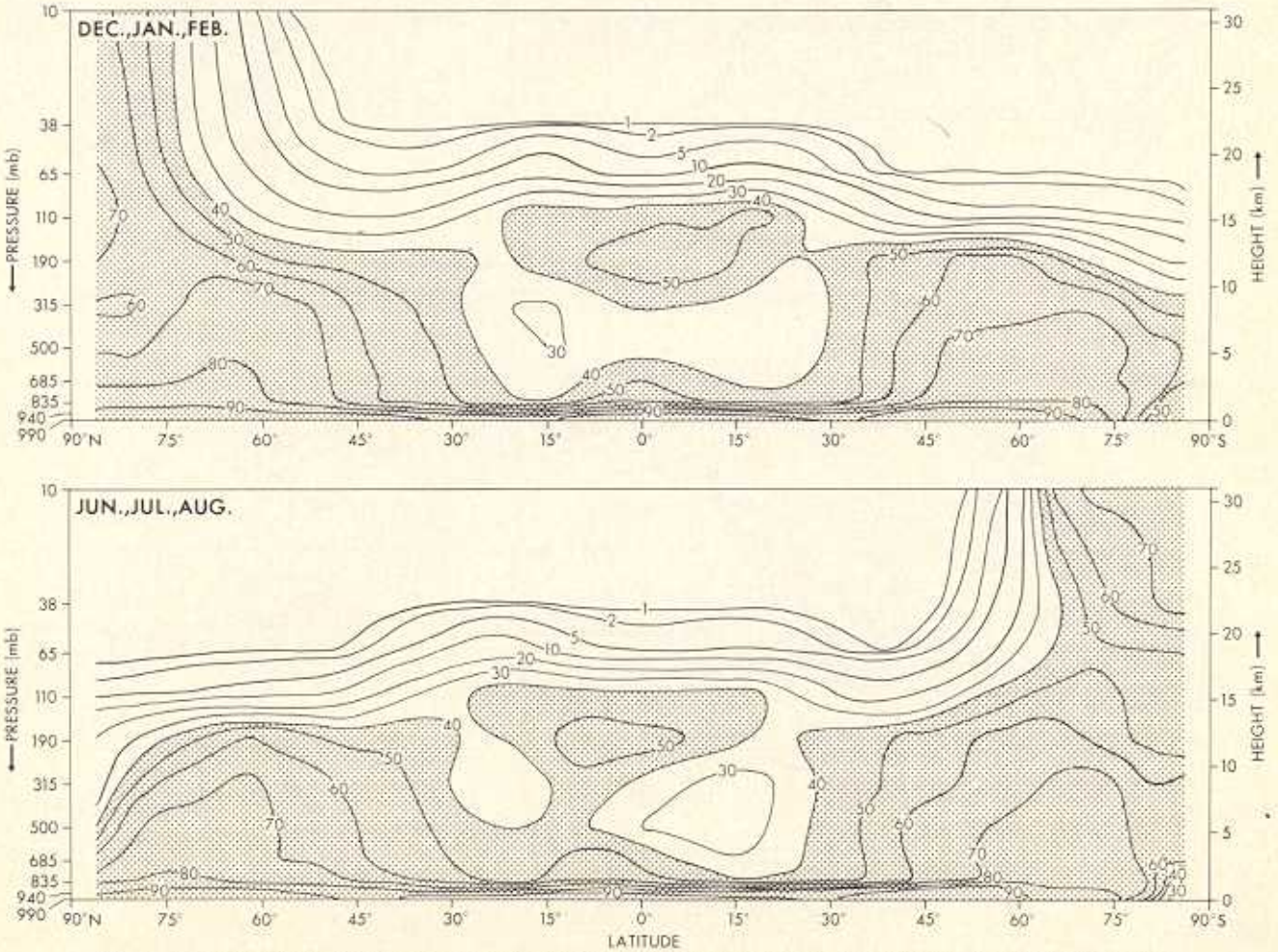

Fig. 9. Latitude-height distributions of zonal-mean simulated relative humidity for December, January, and February (top) and for June, July, and August (bottom) in percent.

in the Hadley cells in the tropics spreads poleward just below the tropopause, creating a layer of high relative humidity in the upper troposphere of the model, in qualitative agreement with *Mastenbrook*'s [1965] observations. On the poleward sides of the Hadley cells, relative humidities are low due to the adiabatic heating in descending air. The humidity is lowest at about 15° latitude of the winter hemisphere, where air descends on the poleward side of the strongest Hadley cell, which straddles the equator. The weaker Hadley cell produces less drying in the opposite hemisphere. The circulating air then flows toward the equator from both subtropical belts, picking up moisture from the earth's surface through evaporation. Thus the Hadley cells create moist layers near the surface and high in the tropical troposphere.

The relative humidity in the model troposphere increases markedly from subtropics to middle latitudes. The poleward transport of moisture by mid-latitude disturbances (shown in Figure 29) is responsible for the fact that the latitude of the maximum relative humidity is higher than the latitude of the maximum upward motion in the Ferrel cell.

WATER BALANCE

In this section we shall present mean global distributions of various hydrologic variables computed by the seasonal model and compare these with climatic data.

Precipitation. Figure 10 shows a comparison between the computed annual mean precipitation rate and the observed annual rate obtained from the *Mira Atlas* [1964]. According to this comparison the general features of the tropical rain belt are well simulated by the model. For example, precipitation is very intense over the Amazon River basin. A major center of high rainfall rate straddles the equator over the western Pacific and Indian oceans. In the eastern Pacific of the model the northern branch of the tropical rain belt lies just north of the

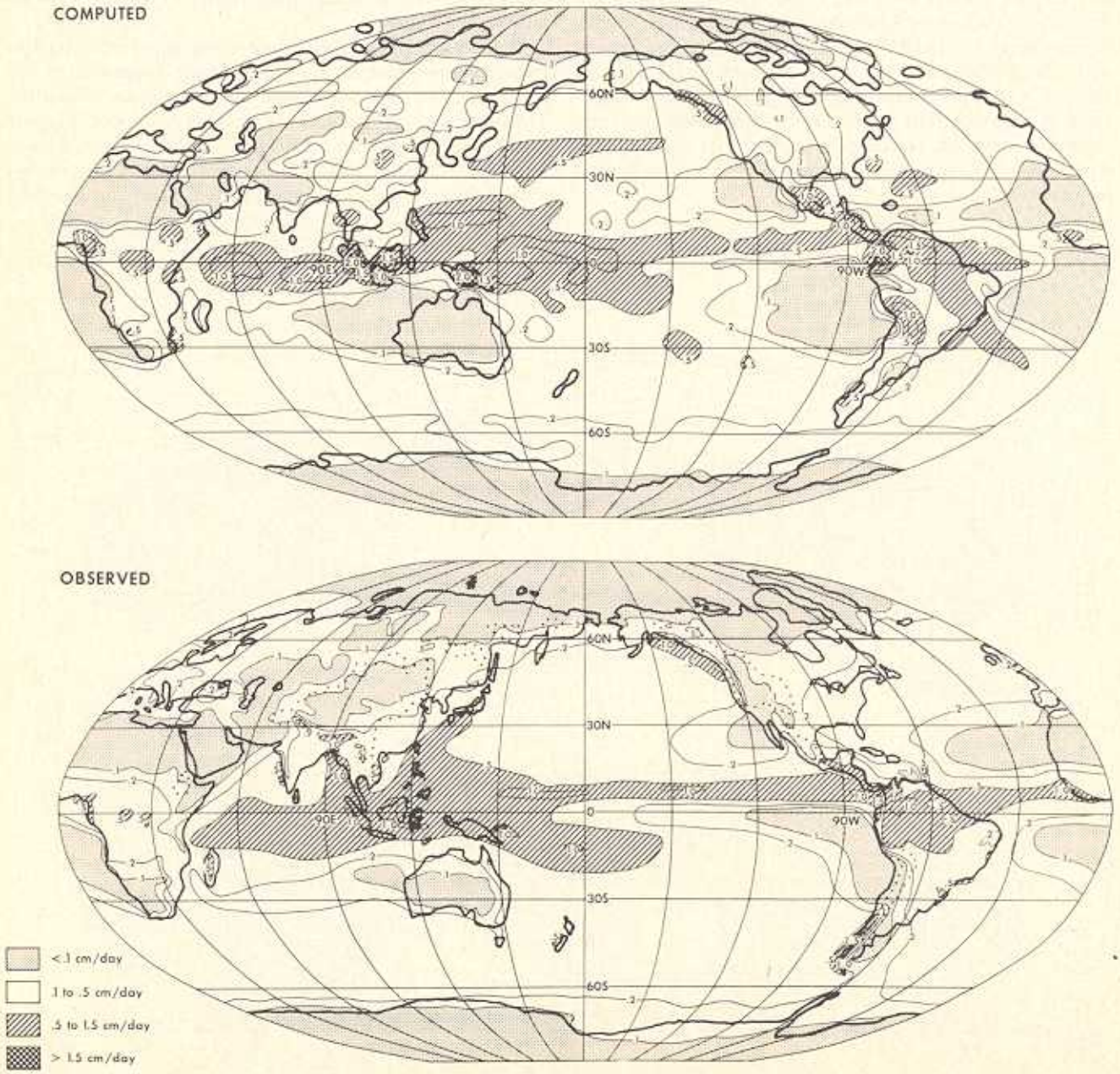

Fig. 10. Global distribution of annual mean rate of precipitation simulated by the model (top) compared with that of the observed annual rate (bottom) derived from the *Mira Atlas* [1964] using some smoothing.

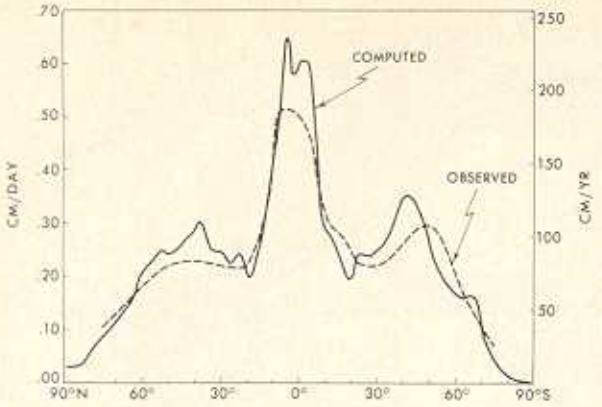

Fig. 11. Latitudinal distribution of the annual mean rate of precipitation computed by model (solid line) and observed [*Budyko*, 1956] (dashed line).

equator, and the southern branch extends toward the southern end of South America. In general, the areas of heavy precipitation in the tropical oceans of the model tropics approximately coincide with regions of warmer sea surface temperature. (See Figure 4.1 in the paper by *Manabe et al.* [1974] for the distribution of the annual mean surface temperature of the model.) On the other hand, rainfall rates are lower where sea surface temperatures are relatively low. For example, on the equator in the eastern Pacific, where upwelling brings cooler water to the surface, rainfall is meager. For further discussion of the relationship between the distributions of sea surface temperature and precipitation rate, see the companion paper by *Manabe et al.* [1974].

In the subtropics of the model the rate of precipitation is generally low because of the adiabatic heating in the downward-moving branch of the Hadley cell. However, it is relatively large along the east coasts of northern hemisphere continents, where the northward advection of the warm and moist air prevails in the summer season. The land–sea surface pressure gradient, which results from the land-sea contrast in surface temperatures, is responsible for the southerly flow along the east coasts of these continents. In the western parts of the continents the model produces areas of very low rainfall rate, such as in the Sahara and in southwestern United States, in agreement with nature. In the subtropics of the southern hemisphere the general features of the distribution of precipitation described above are not as obvious, partly because of the smaller size of the continents. Nevertheless, the model simulates the major arid region in Australia and the belt of moderate precipitation along the east coasts of Australia and Africa. To the west of the continents in the subtropics one generally finds areas of very meager precipitation because of the general downward motion in the semipermanent oceanic anticyclones. *Manabe* [1969] performed a time integration of a model with annual mean insolation and highly idealized geography. He obtained a distribution of precipitation rate in the subtropics which is qualitatively similar to the annual mean distribution described above, and his study contains an extensive discussion of the mechanism by which such a distribution is maintained.

In middle latitudes the rate of precipitation is relatively large, mainly because of the frequent passage of extratropical cyclones. It is particularly large off the east coast of the Eurasian continent as a result of the passage of tropical cyclones and the development of extratropical cyclones. Furthermore, precipitation is enhanced by the rapid evaporation from the warm Kuroshio Current during winter (Figure 16). The precipitation rates along the western slope of the Rocky Mountain range are particularly large around 50°–60°N. A major part of this precipitation occurs during the winter season, as discussed in the latter part of this subsection.

In both the Arctic and the Antarctic region the model specifies low precipitation rates in good agreement with observation. This is consistent with the low water vapor content of the cold air in these regions. In addition, the weak adiabatic heating in a downward-moving branch of the meridional circulation may contribute to the reduction of precipitation there.

Figure 11 gives the computed and observed zonal-mean annual precipitation rates plotted against latitude. Notice that the model reproduces the precipitation maximums in the tropics and in middle latitudes. Likewise, the subtropical minimums in rainfall are simulated. However, there is a tendency for these middle-latitude maximums and minimums to be shifted several degrees toward the equator, especially in the southern hemisphere. This equatorial shift is partly related to the systematic bias of the irregular grid system adopted for this model [*Holloway et al.*, 1973]. The computed precipitation rate in the tropics is significantly higher than the observed rate. This subject is discussed further in the latter part of this section.

The zonal mean of the computed precipitation rate is broken down into averages over land and over sea in Figure 12. It is noteworthy that in the tropics the precipitation rate is greater over land than over sea. This is attributed to the belt of cool sea surface temperatures directly over the equator. For further discussion of this effect, refer to a companion paper [*Manabe et al.*, 1974].

In middle latitudes of the northern hemisphere the computed rate of precipitation over oceans is significantly larger than the rate over continents. Obviously, this results partly from the difference in surface wetness and accordingly from the difference in evaporation rate between land and sea (Figure 18). It should be noted, however, that the difference is mainly a

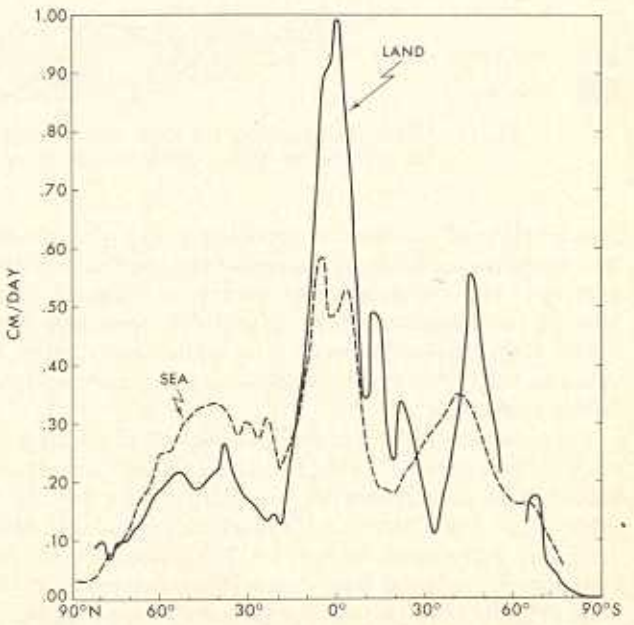

Fig. 12. Latitudinal distribution of the annual mean simulated precipitation rate broken down into zonal means over land (solid line) and over sea (dashed line).

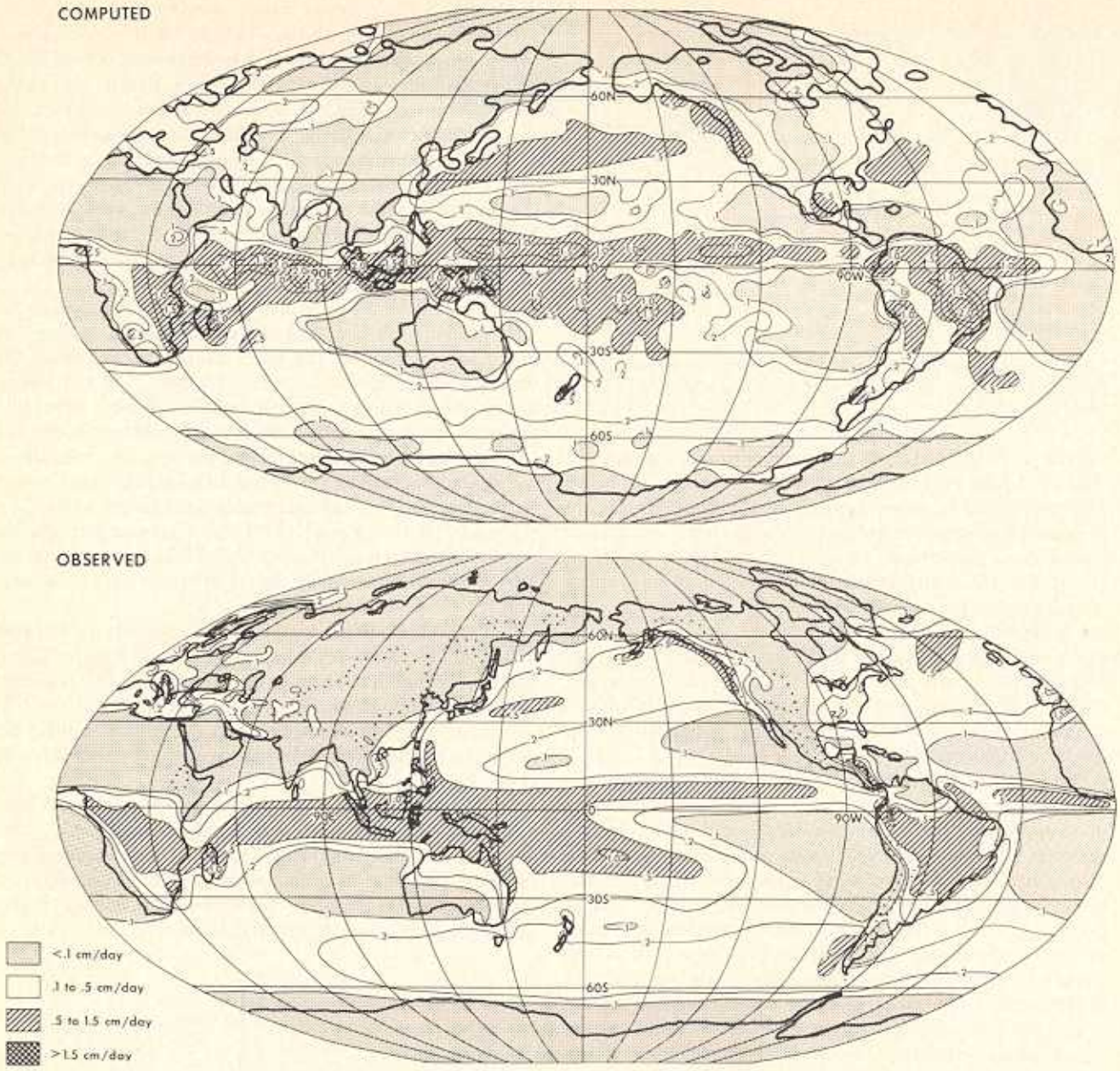

Fig. 13. Global distribution of the mean rate of precipitation computed by the model simulation (top) compared with that estimated by *Möller* [1951] from observed data (bottom) for December, January, and February.

manifestation of the situation prevailing during winter, when the atmospheric circulation suppresses the precipitation over continents and enhances it over oceans, as discussed in the latter part of this subsection. In the southern hemisphere of the model a systematic difference of a similar kind cannot be detected, partly because of the relative small size of continents in this hemisphere.

The seasonal variation of precipitation rate in the model is evident in Figures 13 and 14. These figures present the geographical distributions of precipitation rate for the 3-month periods of December, January, and February and of June, July, and August, respectively. For comparison, the distributions of the actual precipitation rate, estimated by *Möller* [1951] for the same periods, are included in these figures.

According to these figures the latitude of the tropical rain belt in the model changes from season to season. The amplitude of the seasonal shift is particularly large over the continents where the seasonal variation of surface temperature is very pronounced. For example, over Africa and South America in the model the tropical rain belt is located just north of the equator in July but extends from the equator to 30°S in January, in excellent agreement with observation. The belt of heavy precipitation, which is located over the Indian subcontinent in July, shifts back to the equator in January. Although the model successfully simulates this monsoon phenomenon in general, it fails to produce sufficient rainfall in northern India. This failure of the model results from the unrealistically weak monsoon trough, which fails to induce sufficient influx of moist air into the plain region of northern India. For further discussion of this subject, see the companion paper on the South Asian monsoon by *Hahn and Manabe* [1975]. Over the western Pacific of the model the rate of precipitation is very high in July to the north of the equator. As pointed out in the preceding discussions, this belt of heavy precipitation results

from the frequent development of tropical cyclones in this region. In January, tropical disturbances develop in the model over the central and western Pacific Ocean just south of the equator and are responsible for the heavy precipitation there. These features of precipitation distribution are likewise in good agreement with Möller's results shown in the lower halves of Figures 13 and 14.

The seasonal variation of the tropical rain belt is illustrated very clearly in Figure 15, which portrays the latitude-time distributions of the zonal-mean rate of precipitation over continents and oceans separately. As discussed by *Manabe et al.* [1974], the location of the tropical rain belt over oceanic regions of the model approximately follows the belt of warmest sea surface temperatures, in agreement with the findings of *Bjerknes et al.* [1969]. Over the continents the amplitude of the migration of the tropical rain belt is much larger than over the ocean, as pointed out already. This is related to the large latitudinal amplitude for the seasonal motion of the thermal equator on continents. For further discussion of the movement of tropical rain belt, see the companion paper by *Manabe et al.* [1974].

In the subtropics of the model, several regions experience low precipitation rates during both winter and summer. For example, the Sahara Desert and the Australian Desert have little rainfall in either winter or summer. The rate of precipitation is also very low in the neighborhood of the Great Western Desert in North America. This region of meager rainfall, however, extends too far into Texas, as compared with the observed distributions. We speculate that the failure of the finite difference formulation to treat the Rocky Mountains properly may have something to do with this difficulty. Over the eastern part of the oceans the rate of precipitation in the subtropics is very small throughout the year as a result of the general downward motion in the oceanic anticyclones which are situated there (Figure 5). Although precipitation is generally low in the subtropics, where the downward branch of the

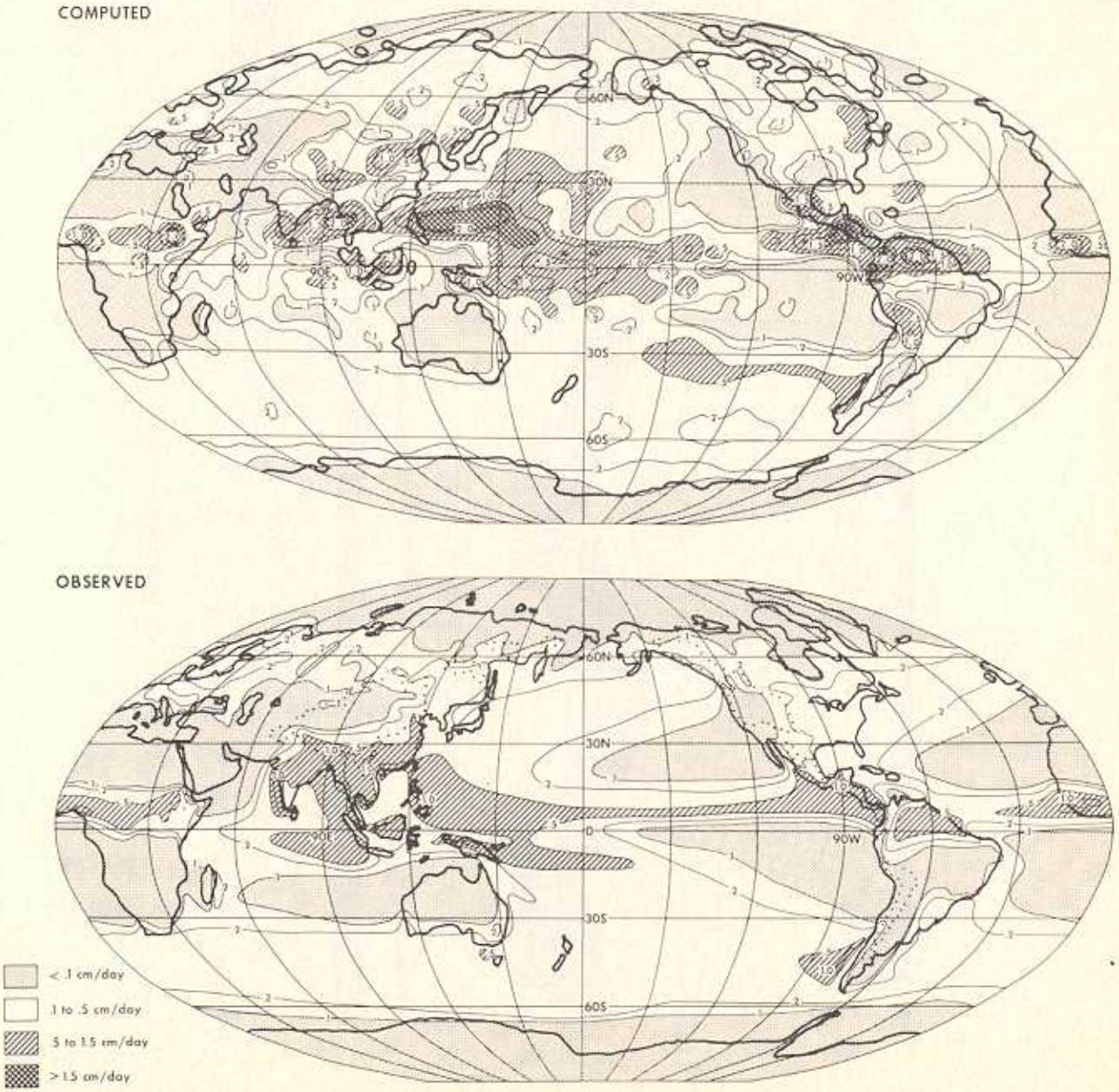

Fig. 14. Same as Figure 13 but for June, July, and August.

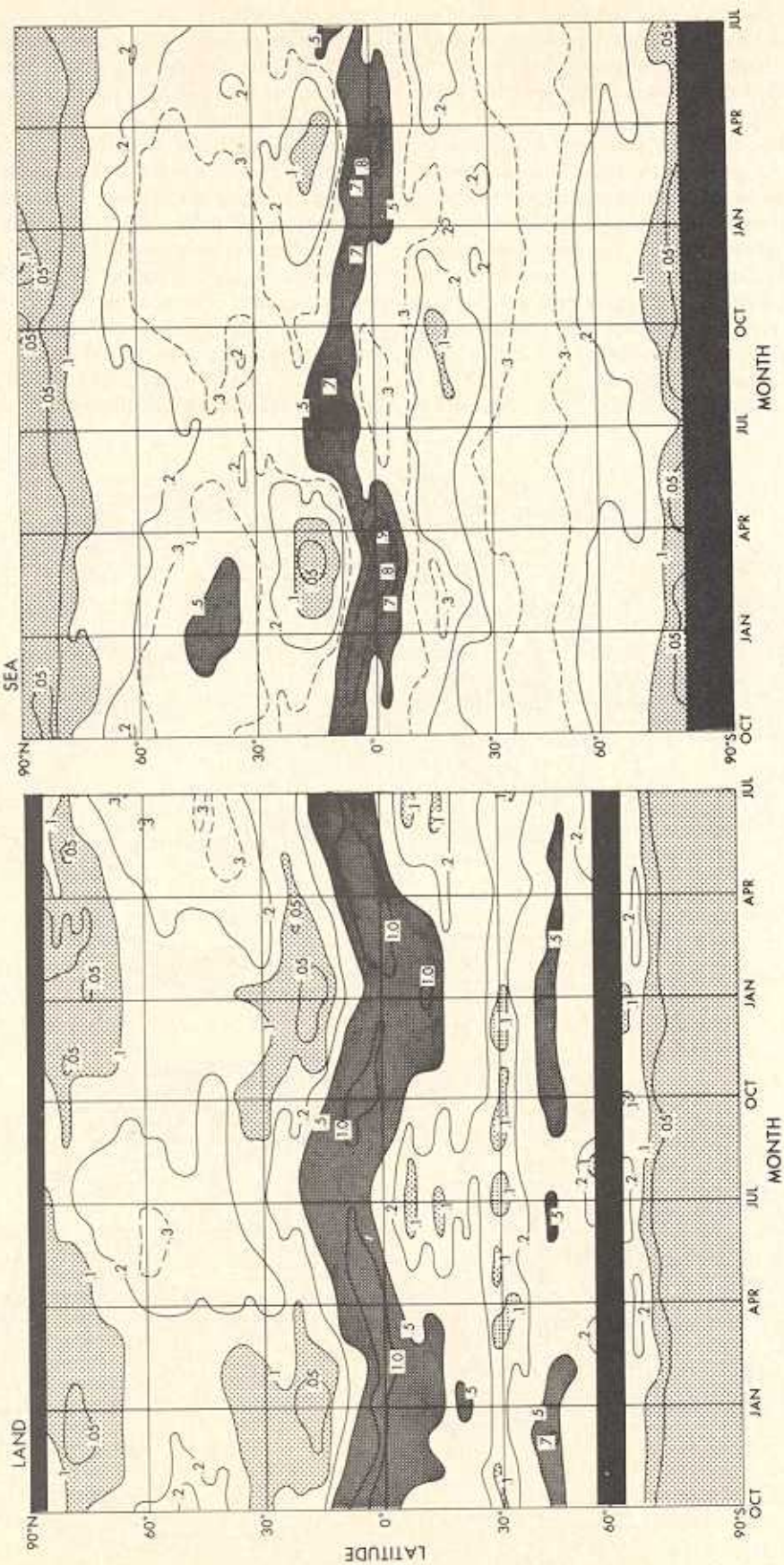

Fig. 15. Latitude-time distribution of the zonal-mean rate of precipitation over land (left) and sea (right) in centimeters per day.

Hadley cell is located, there are some exceptions. In July, precipitation rates are relatively high along the east coasts of the Eurasian and North American continents. In the southern hemisphere, rainfall rates are relatively high along the east coasts of Africa and South America in January. As pointed out already, the poleward advection of moist air along the periphery of the oceanic anticyclones is partly responsible for this phenomenon. Furthermore, it is found that intense tropical cyclones frequently move northward off the east coast of the Eurasian continent during the summer season and bring heavy precipitation to this area.

The seasonal variation of zonal-mean precipitation rate in the subtropics of the model is likewise very evident in Figure 15. According to this figure the precipitation rate in the subtropics is at a minimum in winter over both continents and oceans. This result is consistent with the fact that the downward-moving branch of the most intense Hadley cell is located in the subtropics of the winter hemisphere (Figure 8). It is reasonable that the area of low precipitation rate is more extensive over the continents than over the oceans. Over the continents the meager precipitation produces an area of dry soil. The low evaporation rate in such regions suppresses further precipitation. A similar positive feedback mechanism does not exist over the oceans, which always have a sufficient supply of moisture for evaporation.

Returning to Figures 13 and 14, we see that in middle latitudes of the model the rate of precipitation is very small over most of the Eurasian continent in winter because of the general downward motion in the anticyclone located over this continent. It is particularly small in the eastern part of the continent, where cold and dry northerlies prevail as indicated by the sea level pressure map of Figure 2. On the other hand, a moderate amount of precipitation falls during summer over Siberia, Europe, and the eastern part of the continent. In the

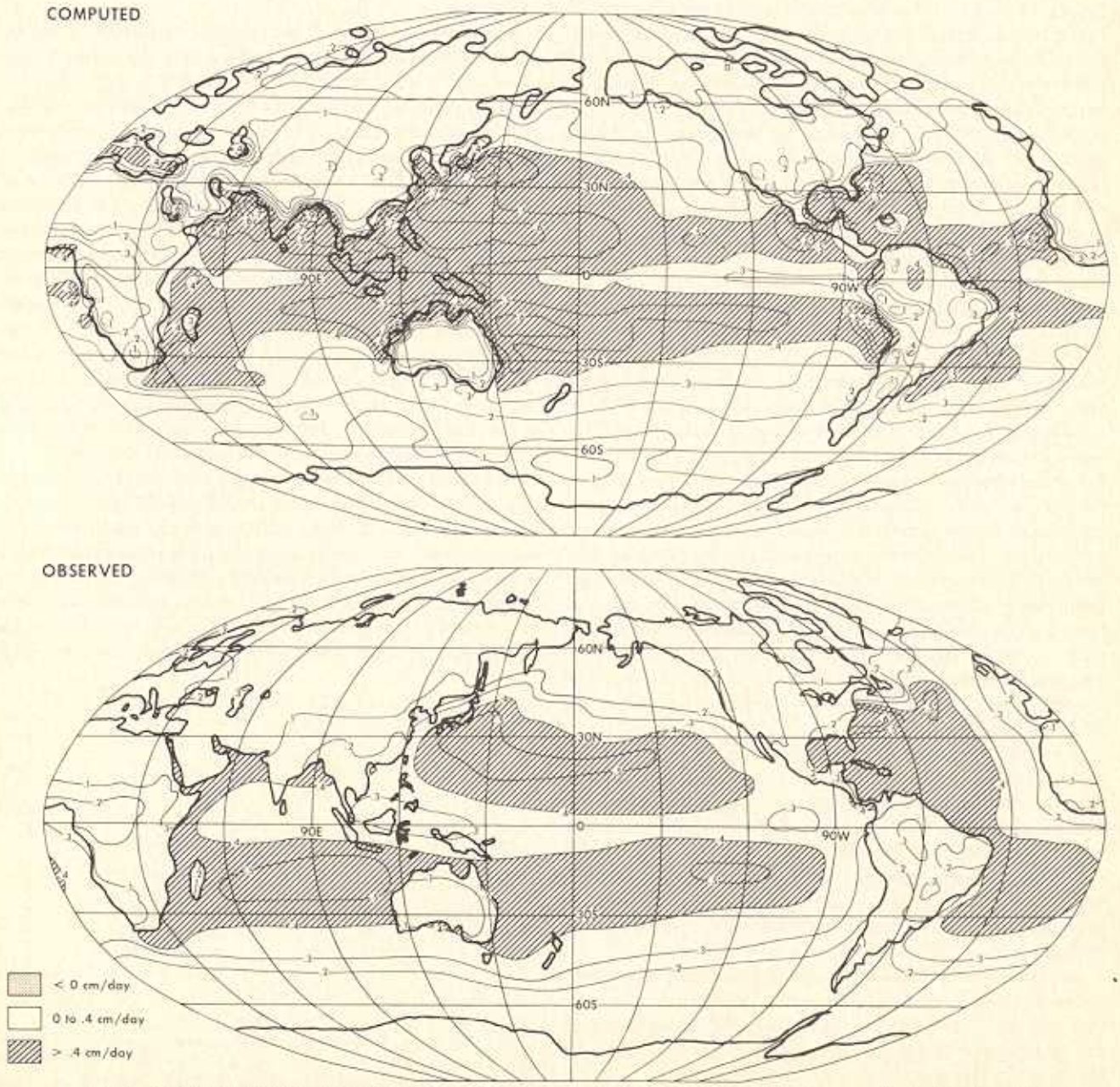

Fig. 16. Global distribution of annual mean rate of evaporation simulated by the model (top) compared with that derived by *Budyko* [1963] from observed data (bottom).

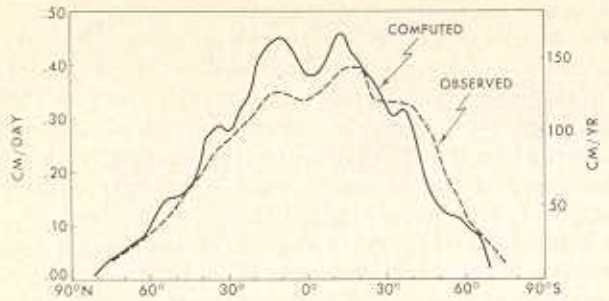

Fig. 17. Latitudinal distribution of annual mean rate of evaporation computed by model (solid line) and derived from observed data [*Budyko*, 1963] (dashed line).

central part of the continent the arid region extending from the Sahara northeastward is identifiable throughout the year, although it is not as extensive as the observed region. Over North America in the model, precipitation rates are very low in the central parts of the United States and Canada in winter, which is due to the subsidence of very dry air in these areas of relatively high surface pressure. Along the western slope of the Rocky Mountains the precipitation rate is very high as a result of the orographic lifting of maritime air flowing northward around the Aleutian low (Figure 5). In summer, moderate amounts of precipitation fall over most of North America, except the southwestern part. These features of precipitation over North America in the model are similar to the features of the observed distribution with the exception of the low-precipitation region around Texas mentioned earlier.

Referring again to Figure 15 one finds that in middle latitudes of the northern hemisphere the rate of precipitation over the model continents is at a maximum in summer and at a minimum in winter. However, over the model oceans the variation in precipitation rate is almost out of phase with the continental variation described above. During winter the moisture content of the continental air masses of the model is low mainly because of low temperatures. Furthermore, surface pressure is relatively high over the model continents and is responsible for the general downward motion and thus meager precipitation there. On the other hand, cyclones develop over the north Pacific and north Atlantic oceans (Figure 4) and thus bring heavy oceanic precipitation. During summer the continental regions of the model are characterized by low surface pressure, moist air, and moderately high precipitation rate, whereas relatively high surface pressure appears over the model oceans, and, accordingly, precipitation rates are relatively low there.

In the southern hemisphere of the model the amplitude of the seasonal variation in the rate of precipitation is much less than that in the northern hemisphere. These interhemispheric differences seem to be due to the small size of the continents relative to the extent of the oceans in the southern hemisphere.

In polar regions, precipitation is meager throughout the year. This is due in part to the general downward motion prevailing there and in part to the low moisture content of the cold polar air.

As mentioned previously, there is good correspondence between the distribution of precipitation described in this section and that of the kinetic energy of the transient eddies shown in Figure 4. For example, in the northern hemisphere the area of high precipitation rate, which extends from Japan to the northwest coast of North America in winter, corresponds well with an area of large eddy kinetic energy. One can detect a similar correspondence off the east coast of North America and in Europe. In the southern hemisphere the zonal belt of relatively high precipitation rate coincides well with that of large eddy kinetic energy in middle latitudes. In the tropics and subtropics the areas of intense precipitation rate approximately agree with those of relatively large eddy kinetic energy, as described extensively by *Manabe et al.* [1974]. For example, note the correspondence in the Philippine Sea during the northern hemisphere summer and in the central Pacific during the southern hemisphere summer. In short, precipitation rate is relatively high in the areas of intense cyclone activity, where eddy kinetic energy is great and intense vertical motion predominates. In the model tropics, precipitation is not only a consequence of cyclonic activity but is also mainly responsible for its maintenance. It has been demonstrated that the conversion of available potential energy generated by the heat of condensation accounts for the major portion of the production of eddy kinetic energy in the model tropics [*Manabe et al.*, 1970].

Evaporation. In Figure 16 the global distribution of the annual mean rate of evaporation computed by the model is compared with values derived by *Budyko* [1963] from observed data. In good qualitative agreement with Budyko's distribution, the maximum computed rate of evaporation occurs in the oceans of the subtropics, especially in the western parts of these ocean basins, where the water is warmest. A band of minimum evaporation occurs on the model earth along the equator between the subtropical belts in the two hemispheres. This equatorial strip of relatively low evaporation rate results from cooler sea surface temperatures directly at the equator than at adjacent latitudes to the north or south. In middle latitudes the evaporation rate is greatest along the east coasts of continents, where the warm ocean currents, such as the Kuroshio Current or the Gulf Stream, prevail. At high latitudes of both hemispheres, evaporation rates are computed to be lowest because of low sea surface temperature (or weak insolation available for the latent heat of evaporation).

The zonal mean of the computed rate of evaporation and that derived from observation are plotted in Figure 17 versus latitude. Two maximums in the northern and southern tropics surround a minimum of evaporation at the equator in both the model and Budyko's distributions. However, the computed evaporation is systematically greater than the observed values in the tropics. The greater computed evaporation rate in the tropics can be attributed to greater evaporation over both

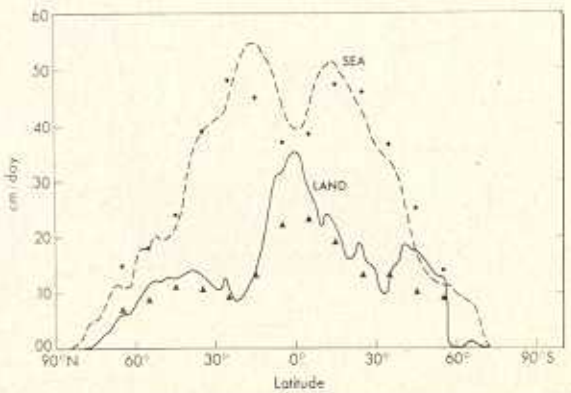

Fig. 18. Latitudinal distribution of simulated annual evaporation rate broken down into means over land (solid line) and over sea (dashed line). For comparison, values for land and sea derived from observed data [*Budyko*, 1963] are indicated by triangles and dots, respectively.

oceanic and continental regions, as indicated by Figure 18, in which evaporation rates are broken down into land and sea values. This figure also indicates that the oceanic evaporation is solely responsible for the double-maximum mentioned above, whereas the evaporation rate over continents is at a maximum directly on the equator. The equatorial belt of relatively low sea surface temperature not only suppresses evaporation but also the development of tropical disturbances and thus reduces the rate of precipitation, as discussed by *Manabe et al.* [1974].

Soil moisture. The amount of soil moisture is essentially controlled by the rate of precipitation and the amount of solar radiation which are available as latent heat for evaporation. This is evident in Figure 19, which shows the global distribution of computed soil moisture. For example, soil moisture is abundant in the equatorial belt of Africa, Indonesia, Central America, and in the Amazon River basin of the model. In these regions the rate of precipitation is so large that it exceeds the high local evaporation rate. The soil is also wet in the subarctic regions such as Siberia and Canada, where the rate of evaporation is small due to the low values of insolation reaching the ground surface. On the other hand, soil moisture of the model has very low values in areas of meager precipitation and abundant insolation, such as in the Sahara Desert and the Australian Desert. Figure 19 indicates that the model is also capable of simulating other arid regions of the world to some degree. For example, the axis of the band of dry terrain running from the Arabian Peninsula to Mongolia in central Asia is well positioned by the model, but the width of this dry area is too small. An offshoot of this area of low soil moisture extends too far south into northern India because the monsoon rainfall is unrealistically low in the plains of India, as pointed out earlier. The model's North American steppe region in southwestern United States is too small, whereas the model creates a region in southern United States which is entirely too dry due to meager precipitation.

The width of the Asian arid soil belt would probably have been much wider in the model if the specified field capacity of the simulated surface had not been as great as the 15 cm chosen for all ground throughout the world. The sandy soil of the desert tends to have a much lower water-holding ability than the soil in wetter regions. A greater-than-actual capacity in arid regions has the effect of prolonging the period during which the soil has moisture and can support evaporation after the infrequent rains in these areas. Longer durations of evaporation support greater precipitation in the model arid areas, which in turn would tend to increase soil moisture.

A close examination of Figure 19 reveals that the model correctly simulated some features of localized areas. For example, in the model the dry regions of Australia do not extend to the east coast of the continent but leave a narrow strip of relatively wet ground along the east and southeastern edges of this country. The southeastern tip of South Africa is also moist, in good agreement with the actual situation there. However, the detailed features of the distribution of soil moisture in South America are not satisfactorily simulated, mainly because of the difficulty in dealing with flow around the narrow and steep Andes Mountain range.

The global distributions of soil moisture during two seasons of the year are shown in Figure 20. In general, they are consistent with the seasonal variation of precipitation rate described in the preceding section. It was decided not to discuss this figure in detail because it is understandable in the light of the discussions of other hydrological quantities presented in this paper.

Runoff. Over the long term, runoff results from the excess of rainfall (and snowmelt) over evaporation. Therefore the success of a model in simulating the distribution of runoff depends very much upon its skill in simulating the distributions of precipitation and evaporation, discussed in the preceding subsections.

The global distribution of the annual mean rate of runoff is compared in Figure 21 with the observed runoff rate derived by *Lvovitch and Ovtchinnikov* [1964]. In general, regions of large runoff rate correspond to areas of heavy precipitation, particularly in the tropical rain belt. For example, the model computes a high rate of runoff in equatorial Africa, in

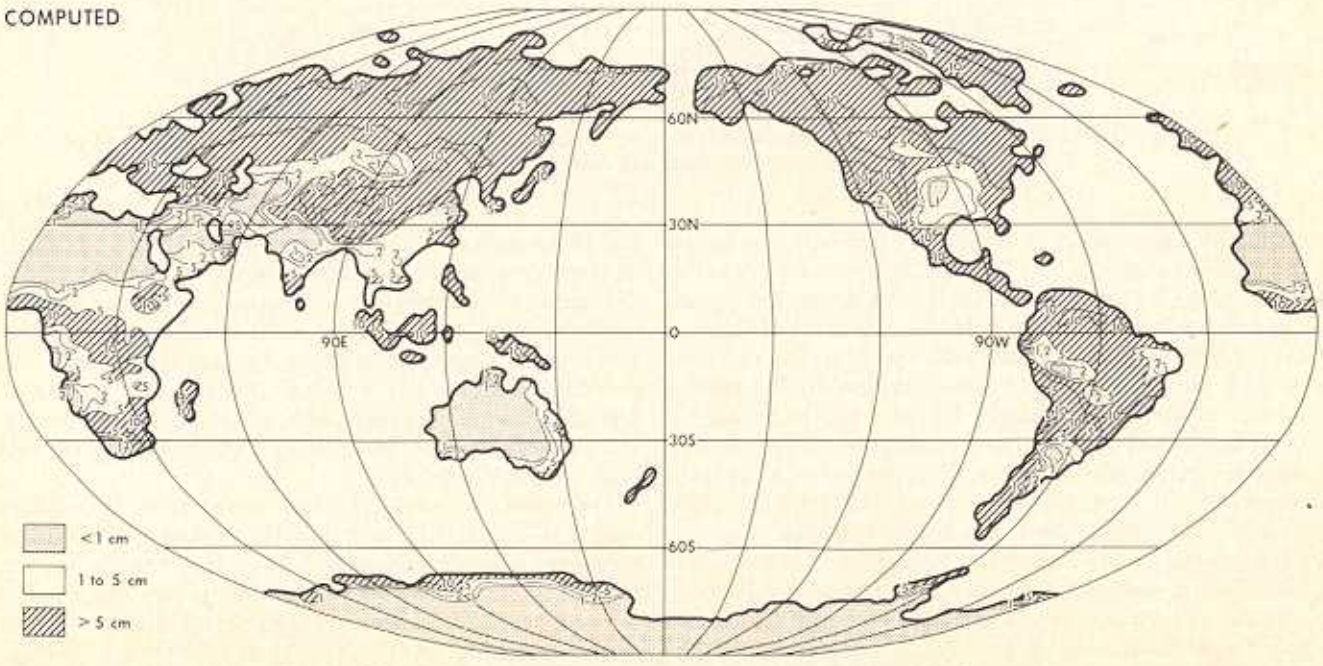

Fig. 19. Global distribution of annual mean soil moisture simulated by the model.

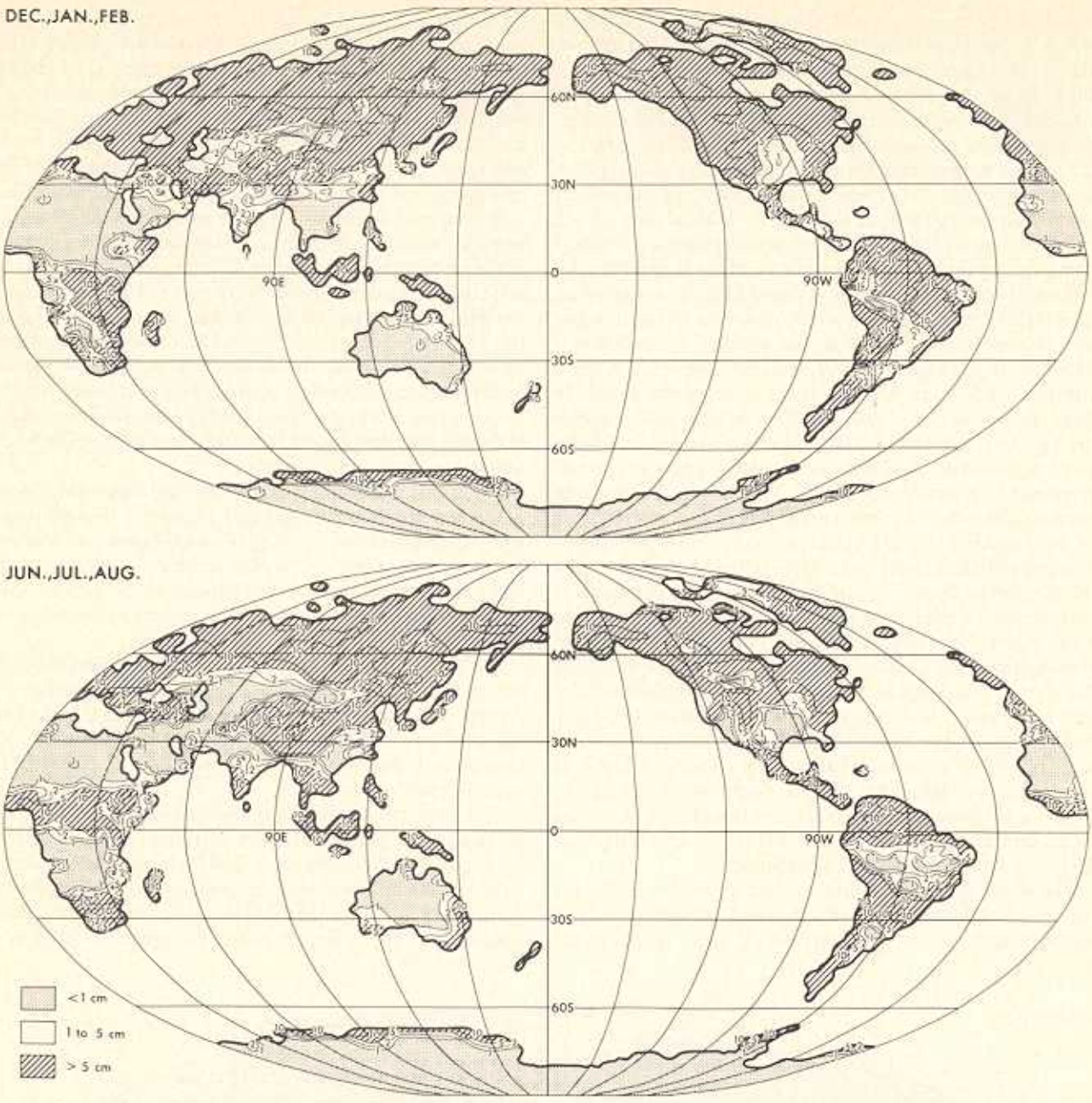

Fig. 20. Global distributions of model-computed soil moisture. Mean for December, January, and February (top) and mean for June, July, and August (bottom).

qualitative agreement with the distribution of the observed runoff. The watersheds for the Congo and Niger rivers and the source of the Nile River are located in this region. The model-simulated high rate of runoff in Indonesia and the Philippines qualitatively agrees with observation. In the tropics of South America the Amazon River basin is simulated by the model.

Most of the regions specified by the model as having no significant runoff approximately coincide with the areas of meager precipitation, with the exception of high latitudes where runoff is not negligible because of the low evaporation rates. For example, runoff is completely missing from the region of the Sahara Desert and the deserts of the Arabian Peninsula, as well as from most of Australia, in agreement with observation. On the other hand, the large area of no runoff in the deserts and steppes of central Asia is significantly narrowed in the model results. The small areas of low runoff rate in Argentina are simulated by the model, as well as a part of the dryness of the watershed in southwest Africa.

In general, the model fails to simulate the observed distribution of runoff in the regions where its simulation of precipitation rate is poor. For example, the model markedly underestimates the rate of runoff in southeastern China, southern United States, and northern India, and it fails to simulate the small-scale features of the distribution of runoff along the west coast of South America.

The model successfully reproduces moderately large runoff over Canada, Siberia, and Europe. Although the rate of precipitation is not very large in these high-latitude regions, the rate of evaporation (or sublimation) is very small due to the weak insolation available. Therefore a substantial amount of water is available in the watersheds of many major rivers, such as the Mackenzie, Ob, Yenisei, and Lena.

Significant parts of the runoff occurring at high latitudes or at high altitudes in middle latitudes can be attributed to snowmelt in the spring. A comparison of the annual global distribution of computed runoff in Figure 21 with the global distribution of annual mean rate of snowmelt, shown in Figure 22, reveals that this is also true in the model simulation. For example, the high rate of runoff on the west coast of Canada and the southern coast of Alaska is associated with the center of the high snowmelt rate centered in the Rocky Mountains of western Canada. Likewise, the snowmelt on the Tibetan Plateau contributes to the center of the large runoff rate north of India where the Indus and Ganges rivers originate. The only significant area of snowmelt in the southern hemisphere is over the Andes Mountains in South America. The high rate of snowmelt here is probably the chief contributor to the excessive runoff rate computed in this area by the model.

Budget of soil moisture. The water budget over continental surfaces of the model is illustrated in the upper part of Figure 23, which includes various components of the budget, i.e., rainfall, snowmelt, evaporation, and runoff. For the sake of comparison, the actual distributions of these quantities, as estimated by *Lvovitch and Ovtchinnikov* [1964], are shown in the lower half of the figure. Notice that in the observed results the distributions of rainfall and snowfall are not shown separately, but only the rate of precipitation (i.e., the sum of rainfall and snowfall) is given. Excluding very high latitudes, where snow gradually transforms into glaciers, snow cover eventually melts and contributes to the runoff. Therefore the rate of precipitation should be approximately equal to the sum of the rates of evaporation and runoff in the long term.

According to the comparison in Figure 23, tropical rain is far too heavy over the continents of the model compared with

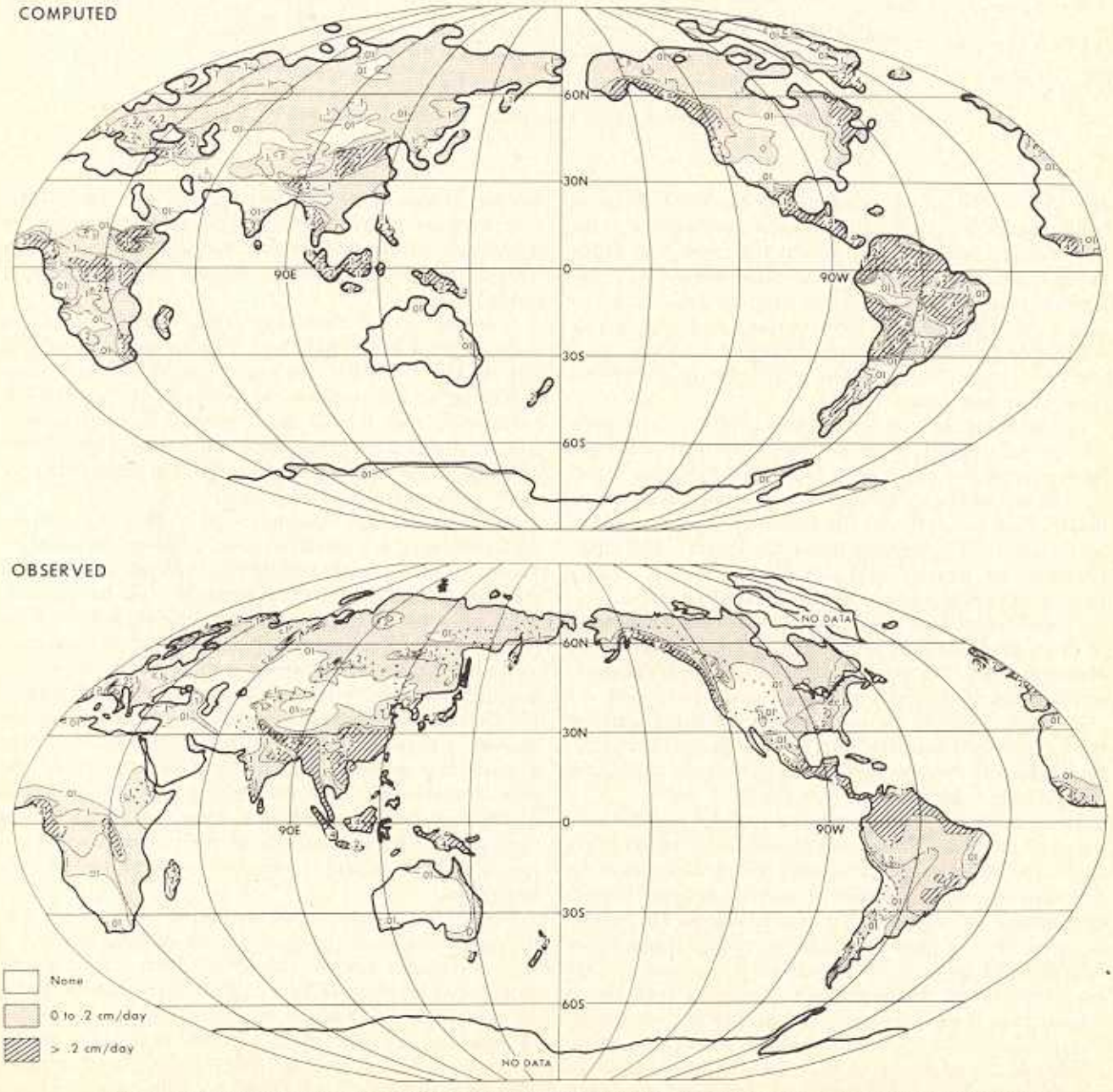

Fig. 21. Global distribution of annual mean rate of runoff simulated by the model (top) compared with an observed distribution (bottom) based on data derived from *Lvovitch and Ovtchinnikov* [1964] using some smoothing.

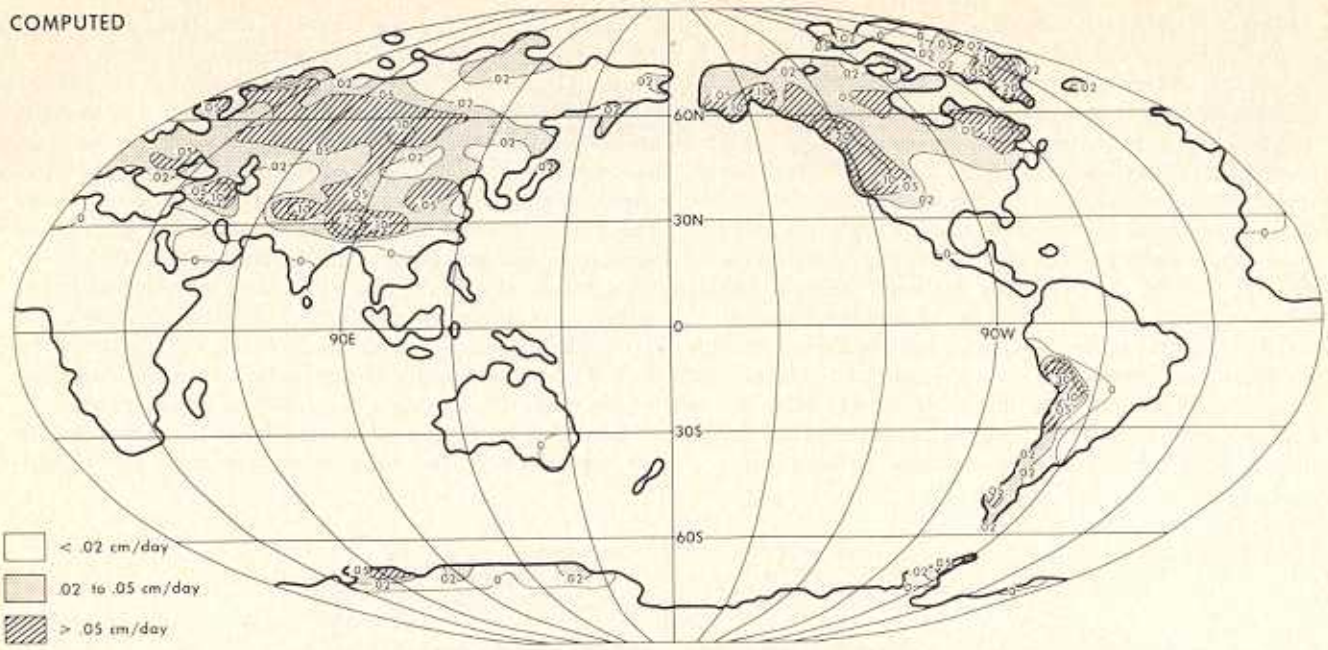

Fig. 22. Global distribution of annual mean rate of snowmelt simulated by the model.

observation. This greater rain results in greater runoff in the model tropics. Notice that the computed evaporation in the tropics agrees with observation, but the runoff rate in the model is nearly double the rate of evaporation. This is opposite to that observed over the continental areas in the actual tropics. Although the estimate of the true runoff in the tropics may not be very accurate, Figure 23 suggests that the model tends to exaggerate the amount of runoff over the tropical parts of the continents.

In the subtropics of the model, precipitation is meager and is almost compensated by evaporation. The small difference between these two components accounts for very low runoff rates in the subtropics, in qualitative agreement with the estimate of the actual runoff. Quantitatively, the magnitude of computed runoff is significantly less than that of actual runoff estimated by *Lvovitch and Ovtchinnikov* [1964], mainly because of the difference in the rate of precipitation.

In middle latitudes the magnitudes of various components of the water budget of the model are much closer to the observed values. The gain of water through rainfall is nearly compensated by the loss due to evaporation and runoff.

In high latitudes of the northern hemisphere the contribution of snowmelt becomes comparable with that of rainfall. Near the South Pole, no liquid water exists in the model, and therefore the water budget is zero there.

The seasonal variation of the water balance over the continents of the model can be investigated by referring to Figures 24, 25, and 26, which present latitude-time distributions of the simulated seasonal variation of zonally averaged runoff, evaporation, and snowmelt rates over land areas. The remaining component of the water budget is rainfall. However, the time graph of rainfall is not shown here for brevity, since the land precipitation graph of Figure 15 may be used instead because rates of rainfall and precipitation are almost identical except at high latitudes, where snowfall accounts for a significant proportion of the precipitation. (In interpreting Figure 26 one must take into account the effects of a computer program error which, unfortunately, remained in the model until the first part of May of the last simulated year. As a result of this error the snow in the model melts almost instantly once the temperature of the snow surface rises above freezing. This error is thought to hasten the removal of snow cover in spring.)

A comparison of these time graphs shows that in the tropics, runoff and evaporation rates are highly correlated with the rate of rainfall. The axes of the maximums of these hydrologic quantities follow the motion of the intertropical convergence zone (ITCZ) near the equator, being farthest north in August and farthest south in February. Therefore the water falling as rain is disposed of almost immediately by runoff or evaporation in the tropics.

In middle and high latitudes of the northern hemisphere, simulated runoff is greatest in spring, as shown in Figure 24. The reason for this is apparent in Figure 26, which shows that the shape and magnitude of the isopleths in the latitude-time graph of snowmelt nearly coincide at these latitudes with the patterns of runoff in Figure 24. Water is stored on the ground as snow in the winter, and when this snow melts in the spring, it contributes to the centers of high runoff rate at this season. The slope of the isopleths of snowmelt is to the upper right, indicating later snow melting with increasing latitude. In the southern hemisphere the runoff rate is high throughout the year. With the exception of the Antarctic continent the rate of runoff does not have a distinct spring maximum, partly because snowmelt is a less important contributor to runoff and partly because rainfall varies less with season in this hemisphere.

Evaporation rate is mainly controlled by insolation and moisture available at the ground. Both of these factors are high in the early summer in middle latitudes, and the time graph of evaporation (Figure 25) illustrates that the model does indeed indicate a maximum evaporation rate at this time of year, i.e., in June in the northern hemisphere and in December in the southern hemisphere. Later in summer the insolation is somewhat weaker, and the ground has been dried out by earlier strong evaporation; therefore the rate of

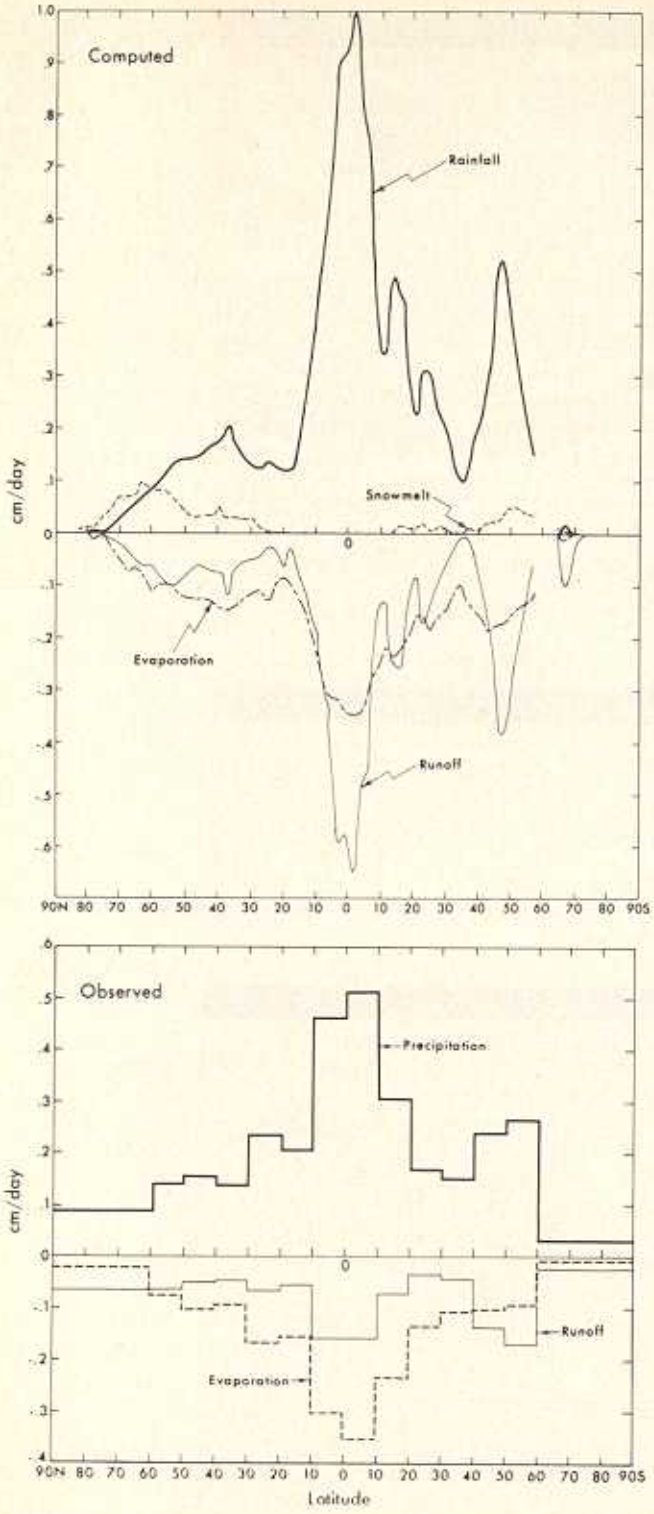

Fig. 23. Zonal-mean components of the water budget over land computed by the model (top) and estimated from observed data by *Lvovitch and Ovtchinnikov* [1964] (bottom).

evaporation decreases from its peak in early summer. In high latitudes the time of maximum rate arrives somewhat later, as one may infer from the preceding discussions.

Budget of snow. The net rate of snow accumulation over land is determined by the rate of snowfall and by the rates of snowmelt and sublimation, both of which decrease snow depth. This is illustrated in Figure 27, which presents the four components of the snow budget over continents. In middle latitudes the contribution of snowfall is very nearly compensated by the sum of the contributions of snowmelt and sublimation. Consequently, there is no net snow accumulation over the long term, with the exception of latitudes having very high mountains, such as the Himalayas or the Andes. In the model the rate of depletion of snow cover by snow melting exceeds that by sublimation by about an order of magnitude. Most of the snow accumulation occurs at high latitudes of both hemispheres. This snow accumulation in nature leads to glacier formation, which is neglected in this model. Therefore snow is allowed to accumulate without bound during the model integration. It is probable that the diurnal variation of insolation enhances snowmelt during daytime and reduces the rate of net snow accumulation. Therefore the neglect of the effects of diurnal variation in the model could result in the overestimation of the rate of snow accumulation, whereas the computer program error mentioned earlier has the opposite effect.

The seasonal variation of snow cover is illustrated in Figure 28, which shows the latitude-time distribution of the zonal mean of the water equivalent of snow cover over the model continents. This figure indicates that the snow cover at high latitudes tends to deepen from one year to the next, as discussed above. In middle latitudes of the northern hemisphere the rate of accumulation of snow during fall is somewhat lower than the rate of snow depletion in spring. In view of the computer program error in the computation of snowmelt discussed earlier, this interesting tendency should be reexamined with a corrected model. Note that in the spring the snow cover in the northern hemisphere subtropics of the model tends to remain later than the snow cover in middle latitudes. This represents the tendency of snow cover over the Tibetan Plateau to persist longer as a result of the low temperatures at high altitude.

Global water budget. Recently, *Baumgartner and Reichel* [1973] compiled a list of estimates of the global mean values of annual mean precipitation by various authors. The most recent estimates contained in their list compared with the annual mean precipitation obtained from the model are given below.

	P ($\approx E$)
Budyko [1963]	100.0
Mira Atlas [1964]	102.0
Mather [1970]	95.5
Budyko [1970]	102.0
Baumgartner and Reichel [1973]	97.3
Present Model	104.1

where P is given in centimeters per year. This comparison indicates that the global mean rate of computed precipitation is somewhat larger than recent estimates of actual precipitation. However, the magnitude of the difference between the computed and the observed values seems to be within the range of variability of the recent estimates of actual precipitation.

In Table 1 the earth's surface is subdivided into simple categories such as oceans and continents or northern and southern hemispheres. The annual mean rates of precipitation and evaporation over each region of the model are tabulated, together with the estimates of these quantities by *Baumgartner and Reichel* [1973].

According to this comparison the largest difference between these two results lies in the rate of precipitation over continents; i.e., the model yields a rate which is about 30% larger than the estimate of Baumgartner and Reichel. On the other hand, the model simulates a rate of evaporation which is very similar to the observed rate. Therefore the difference between

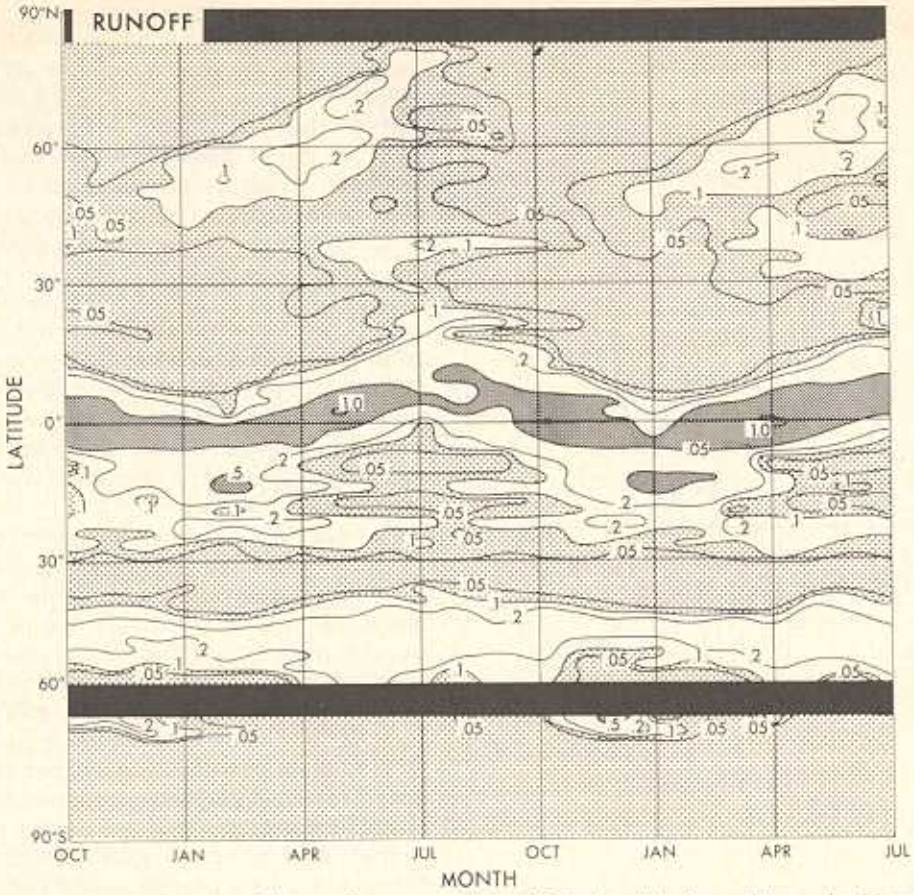

Fig. 24. Latitude-time distribution of the zonal-mean rate of runoff simulated by the model over land in units of centimeters per day.

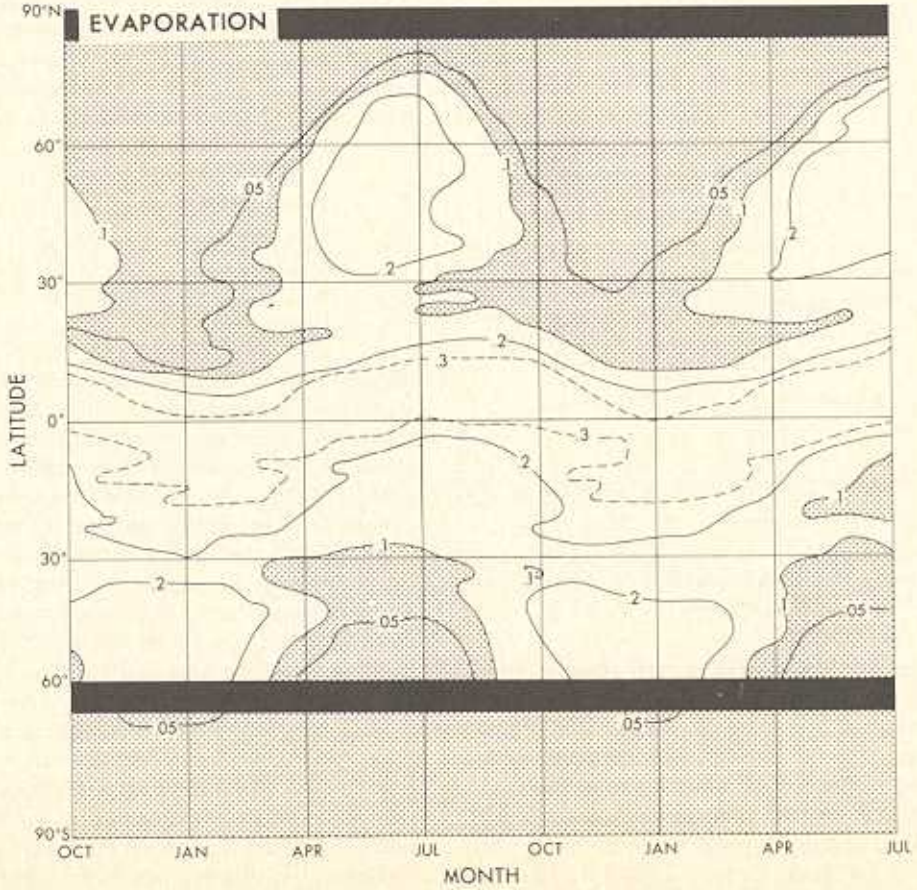

Fig. 25. Same as Figure 24 but for rate of evaporation.

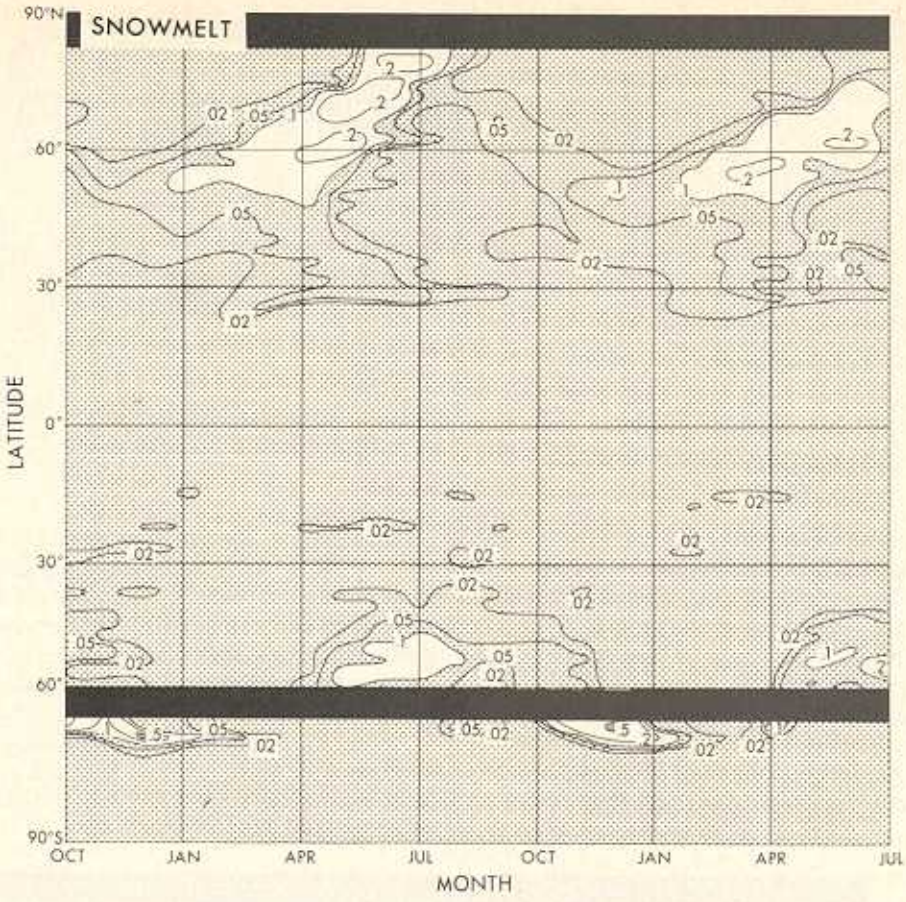

Fig. 26. Same as Figure 24 but for rate of snowmelt.

the rate of precipitation and that of evaporation averaged over the model continents is about twice as large as the estimate of the actual difference. This implies that the runoff over the model continents is nearly twice as large as that over actual continents. As discussed already, the rate of precipitation computed by the model is extremely large over tropical regions of

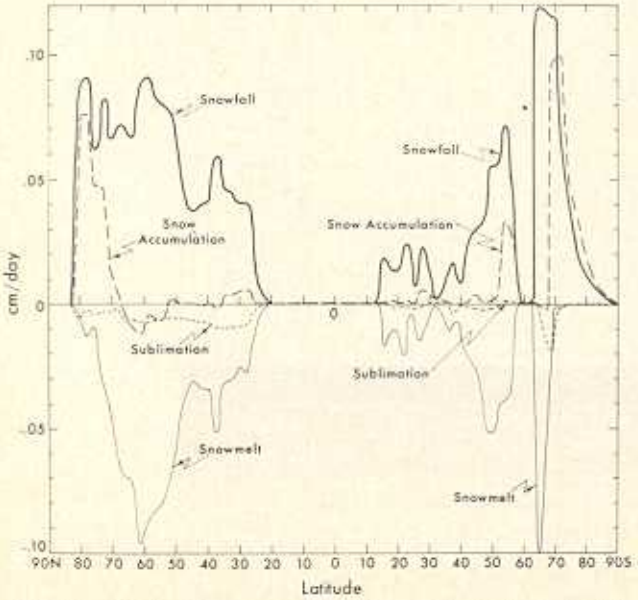

Fig. 27. Zonal-mean components of the snow budget simulated by the model over land. Snowmelt and sublimation are plotted as negative quantities.

continents and accounts for the large difference in the rates of precipitation and runoff mentioned above.

Over the oceanic regions of the model the rate of evaporation is not very different from that of precipitation, in agreement with the results of Baumgartner and Reichel. The small excess of evaporation over precipitation results in the export of water vapor from oceanic to continental regions. On the other hand, continents return the water through runoff. Since the area of oceans is much larger than that of continents, the small negative $(P - E)$ over oceans is sufficient to compensate for the large positive $(P - E)$ over continents, thus maintaining the budget of water vapor in the atmosphere over the entire globe in the long term. Table 1 also reveals that the magnitude of $(P - E)$ over the model oceans is about 1.7 times that over the actual oceans, as estimated by Baumgartner and Reichel.

As a whole the rate of precipitation computed by the model is slightly larger than the rate of evaporation over the northern hemisphere. This result implies that the southern hemisphere, mostly covered by ocean, exports moisture to the northern hemisphere in the model. The magnitude of this computed export, however, is somewhat smaller than the magnitude estimated for the actual atmosphere.

Atmospheric water vapor transport. The water balance of the atmosphere is maintained by processes which transport water vapor from where there is an excess of evaporation over precipitation to regions where precipitation exceeds evaporation. The purpose of this subsection is to point out the mechanisms important to the redistribution of moisture at various latitudes of the earth, as indicated by the model simulation.

Figure 29 presents curves of the zonal-mean values of the

TABLE 1. Annual Mean Precipitation P and Evaporation E Over Various Regions in Units of Centimeters per Year

	Model			*Baumgartner and Reichel* [1973]		
	P	E	$P-E$	P	E	$P-E$
Continent						
Globe	97.2	51.1	46.1	74.8	48.1	26.7
Northern hemisphere	91.7	49.8	41.9	67.9	43.5	24.4
Southern hemisphere	110.3	54.5	55.9	88.5	57.0	31.5
Ocean						
Globe	107.7	126.2	-18.5	106.7	117.7	-11.0
Northern hemisphere	117.0	138.4	-21.3	116.1	120.0	-3.9
Southern hemisphere	99.2	116.7	-17.6	99.5	115.8	-16.3
Earth						
Globe	104.1	104.1	...	97.3	97.3	...
Northern hemisphere	107.0	103.2	3.8	97.0	89.8	7.2
Southern hemisphere	101.3	105.1	-3.8	97.6	104.8	-7.2

model-simulated annual mean northward transport of water vapor by the meridional circulation, by large-scale eddies, and by parameterized subgrid scale diffusion. Plotted on this same graph are values of the first two transports as obtained by *Oort and Rasmusson* [1970] from the observed data north of 10°S. According to this comparison the computed and the observationally derived distributions of eddy transport agree very well with each other. However, the distribution of transport by the meridional circulation in the model atmosphere differs somewhat from that estimated by Oort and Rasmusson. As described earlier, the centers of both the Hadley and the Ferrel cells in the model atmosphere are significantly lower than those obtained by Oort and Rasmusson. Because of the rapid decrease of the mixing ratio of water vapor with height, this difference in the shape of the meridional circulation cells could account for the difference in the magnitude of the transport mentioned above.

Figure 29 shows that the meridional circulation brings moisture into the tropics from the north and south subtropical belts, whereas the large-scale eddies are principally responsible

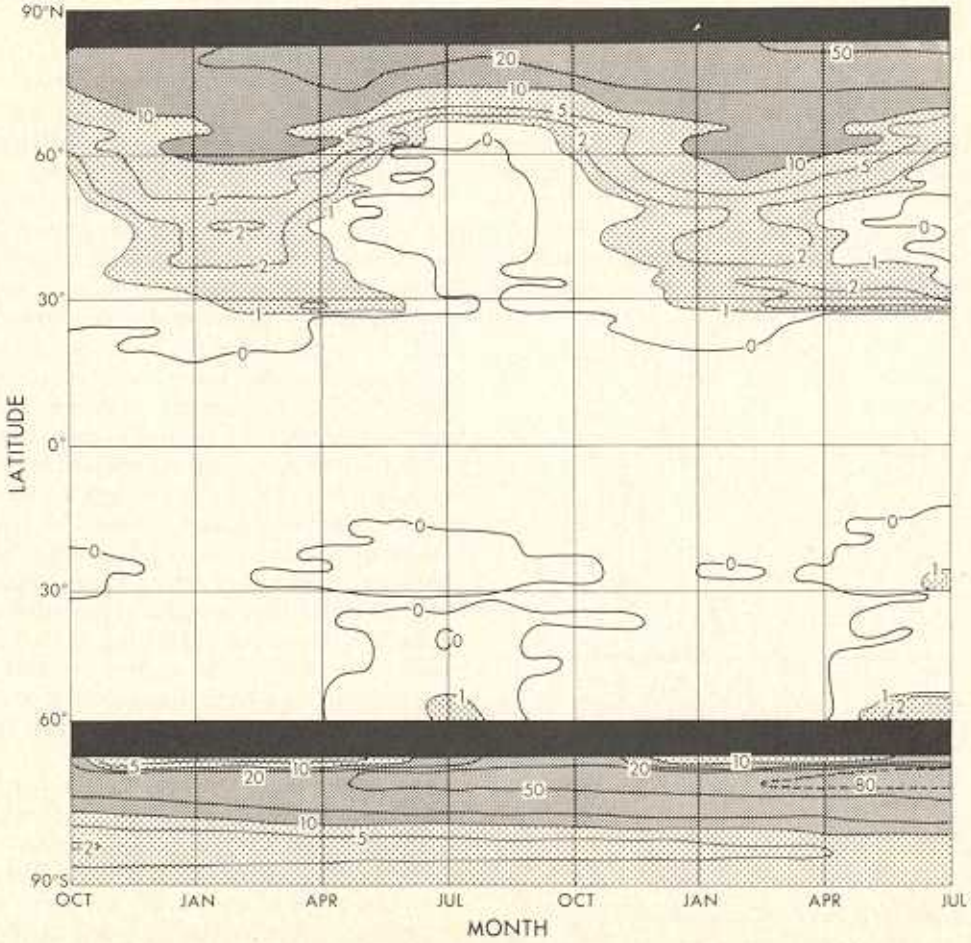

Fig. 28. Latitude-time distribution of the zonal mean of water equivalent depth of snow cover simulated by the model over land in units of centimeters.

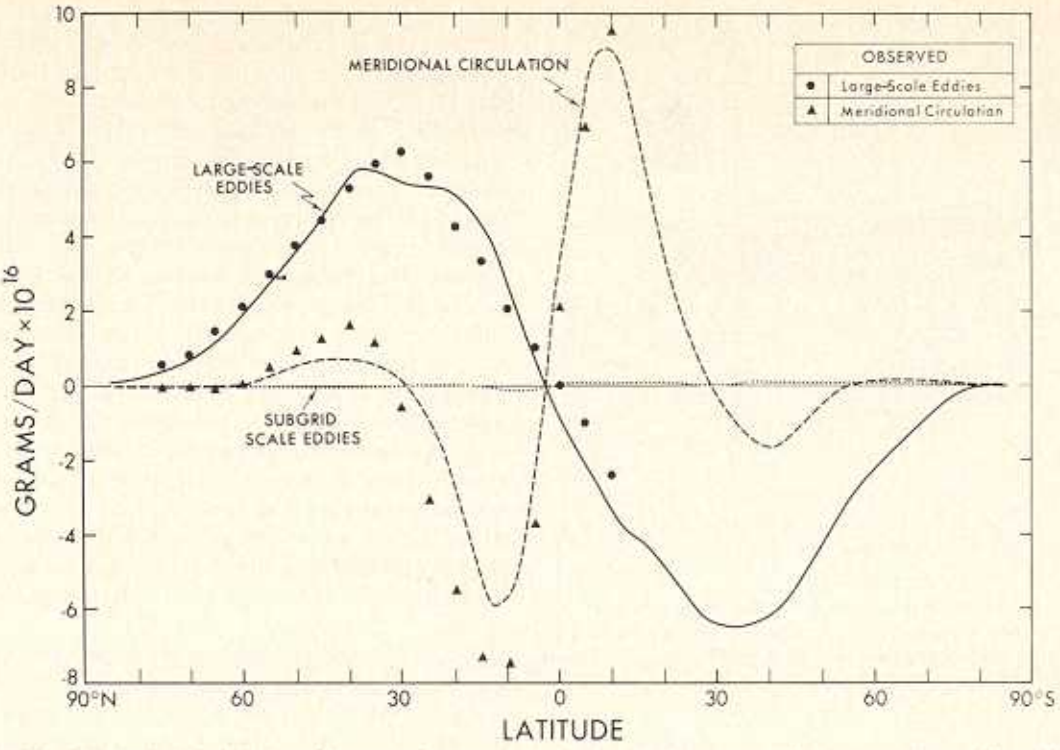

Fig. 29. Latitudinal distribution of the annual mean simulated northward transport of water vapor by meridional circulation (dashed line), by large-scale eddies (solid line), and by subgrid scale eddies (dotted line). Observed values of the first two transports derived by *Oort and Rasmusson* [1970] are plotted on this graph as triangles and dots, respectively.

for transporting water vapor poleward from the subtropics into middle latitudes. The contribution of the subgrid scale eddies is negligible.

The latitudinal distributions of the various components of the annual mean budget of water vapor in the model atmosphere are shown in Figure 30. The components of the budget included in this figure are the contributions of the transport by meridional circulation, by large-scale eddies, and by subgrid scale eddies. Also shown in this figure is the source of water vapor, i.e., the rate of evaporation minus the rate of precipitation.

According to this figure the meridional circulation (the Hadley cell in this case) is responsible for supplying water vapor to the tropical rain belt, where the rate of precipitation far exceeds that of evaporation. The major source region of water vapor is the subtropics, where the meridional circulation plays a major role in exporting water vapor toward other latitude belts. In middle and high latitudes the precipitation rate is significantly larger than the evaporation rate. Large-scale eddies are responsible for supplying water vapor by importing it from lower latitudes.

The seasonal variation of the zonal mean of the northward transport of water vapor is plotted in Figure 31 for the last year of the time integration of the model. Notice that the northward moisture transport across the equator is at a maximum in August. On the other hand, the greatest southward transport of water vapor occurs in February. In either case the moisture transport is being accomplished by the strongest Hadley cell in the tropics, i.e., the one that straddles the equator. See the earlier discussion of the meridional circulation of the model. This interhemispheric Hadley cell carries moisture across the equator into the tropics of the summer hemisphere and supplies water to the high rainfall region along the ITCZ. *Oort and Rasmusson* [1970] have shown that seasonal variations of a similar nature occur in the actual tropics. In middle latitudes, where the poleward moisture transport is at a secondary maximum, the seasonal variation of the transport is relatively small.

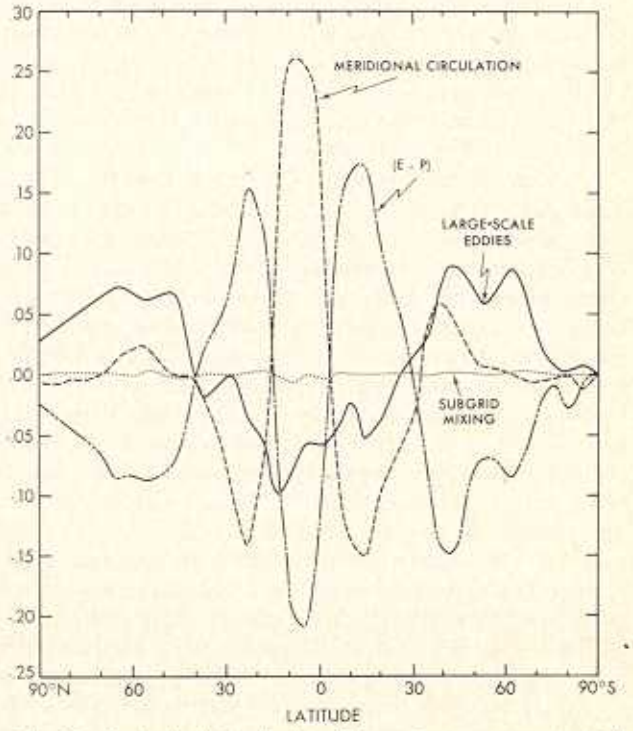

Fig. 30. Latitudinal distribution of the various components of the annual mean budget of water vapor in the model atmosphere in units of centimeters per day. Note that $(E - P)$ signifies difference between evaporation and precipitation rates.

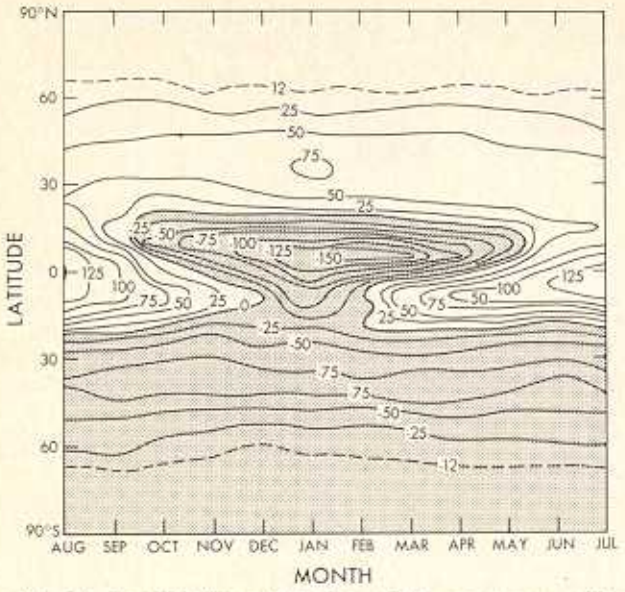

Fig. 31. Latitude-time distribution of the zonal mean of the northward transport of water vapor for the last year of the time integration of the model in units of 10^{15} g day^{-1}. Negative values (southward transport) are shaded.

Simulation of Climate

In the preceding sections the model described in this paper has been shown to be capable of rather accurately simulating the seasonal variation of various climatic elements such as mean temperature and precipitation. Therefore it ought to be possible to determine the climatic type into which a particular region should fall on the basis of the model-simulated meteorological variables. To summarize the climatic simulation ability of this model, the mean seasonal temperature and precipitation have been used to derive a global distribution of climatic groups for comparison with a similar distribution based on observed data. It should be pointed out that this section is included to combine previously reported results from the model simulation into a form more easily evaluated by climatologists.

A widely accepted system of climate classification is that developed by *Köppen* [1931]. In this system, monthly mean temperatures and precipitation amounts are used as criteria for subdividing climates of the earth into five major groups (designated 'A' through 'E') and a number of subtypes. Group A designates tropical rainy climates; B, desert (BW) and steppe (BS) climates; C, wet temperate regions with mild winters; D, wet temperate climates with cold winters; and E, tundra (ET) and perpetually frozen (EF) areas. A lower-case letter following the capital letter for groups A, C, and D delineates the characteristics of the seasonal variation of precipitation rate. In particular, 'f' indicates areas where the precipitation is roughly evenly distributed throughout the year; 'w' or 's' is used when the particular area has a dry winter or dry summer, respectively. Hot or cold climates within the B group are differentiated by lower-case letters 'h' or 'k' following the BW or BS. In C and D groups, the progression from hot to cool summers is indicated by lower case letters 'a' through 'c' following the precipitation distribution notation. A lower case 'd' at the end of D climate designations indicates a very cold winter. The quantitative definition of these climate categories can be found in almost any climatology textbook. We used *Haurwitz and Austin* [1944] and *Trewartha* [1968] for adopting the most widely accepted criteria for deriving the Köppen types from the simulated model results.

In Figure 32 the Köppen climatic groups and subdivisions, derived on the basis of the model simulation, are compared with those based on actual data [*Trewartha*, 1968]. The Köppen climate classification scheme was originally designed to delineate regions by the different types of terrestrial vegetation which they can support, such as trees, grasses, agricultural crops, tundra mosses, and so forth. For this reason, the Köppen climate classes are meaningless over the oceans, where no land plant life grows. Therefore the computed and observed climate groups are shown only over the continents in Figure 32. For simplicity, these maps are shaded according to the precipitation components of the climate types. Arid climatic regions (group B climates) are shaded with dots. Wet climates without a dry season (groups Af, Cf, and Df) are indicated by cross hatching. Regions with monsoon climates and hence dry winters are shaded with diagonal lines (Aw, Cw, and Dw). Areas having a dry summer or Mediterranean climate are shaded with diagonals drawn in the opposite direction. Finally, tundra (ET) and frozen (EF) climate regions are left unshaded.

Figure 32 shows that the tropical rainy climates are well simulated by the model. Notice that in the equatorial regions of South America, Africa, and Indonesia, Af climates are indicated in the computed map in good qualitative agreement with the observed distribution of this climate type. To the north and south of this belt of Af climate are savanna (Aw) and monsoon (Am) climates, in which the weather is relatively dry during the season when the sun is in the opposite hemisphere. North of the Af climate of Indonesia, for example, India, Indochina, and the Philippines are correctly covered by Aw and Am climates. The Am, or tropical monsoon, climate is midway between the Af and the Aw climates in the Köppen classification system, but areas having this climate are shaded the same as Af in Figure 32 because their yearly rainfall amounts more closely match those of Af regions. The distribution of the tropical savanna climate (Aw) in Africa, South America, and Australia is consistent with the seasonal movement of the tropical rain belt discussed earlier. The good simulation of this climate type is merely an indication of the ability of the model to simulate the seasonal movement of the tropical rain belt correctly.

The most successful simulations of subtropical dry climates by the model are in Australia and in northern Africa. Most of the Australian continent is covered by desert (BW) and steppe (BS) climates, and this is well simulated by the model. The wet regions in this country are along the northern coast, where an Aw climate exists, and on the southern and eastern coasts, where C climates prevail. The broad area of deserts in northern Africa is flanked by narrow belts of steppes on the north and south which are transitions into savanna (Aw) regions to the south and a C climate to the north along the Mediterranean coast.

The belt of arid climate extending from the Sahara Desert to deep into central Asia is in general well simulated by the model, although the area of the arid region corresponding to the Gobi Desert is not wide enough. Results from recent numerical experiments, carried out at the Geophysical Fluid Dynamics Laboratory, indicate that the Tibetan Plateau plays a major role in maintaining the arid region in central Asia. For example, *Manabe and Terpstra* [1974] have shown that in a model without mountains the Siberian high is very weak and is located in the southern part of the Eurasian continent in

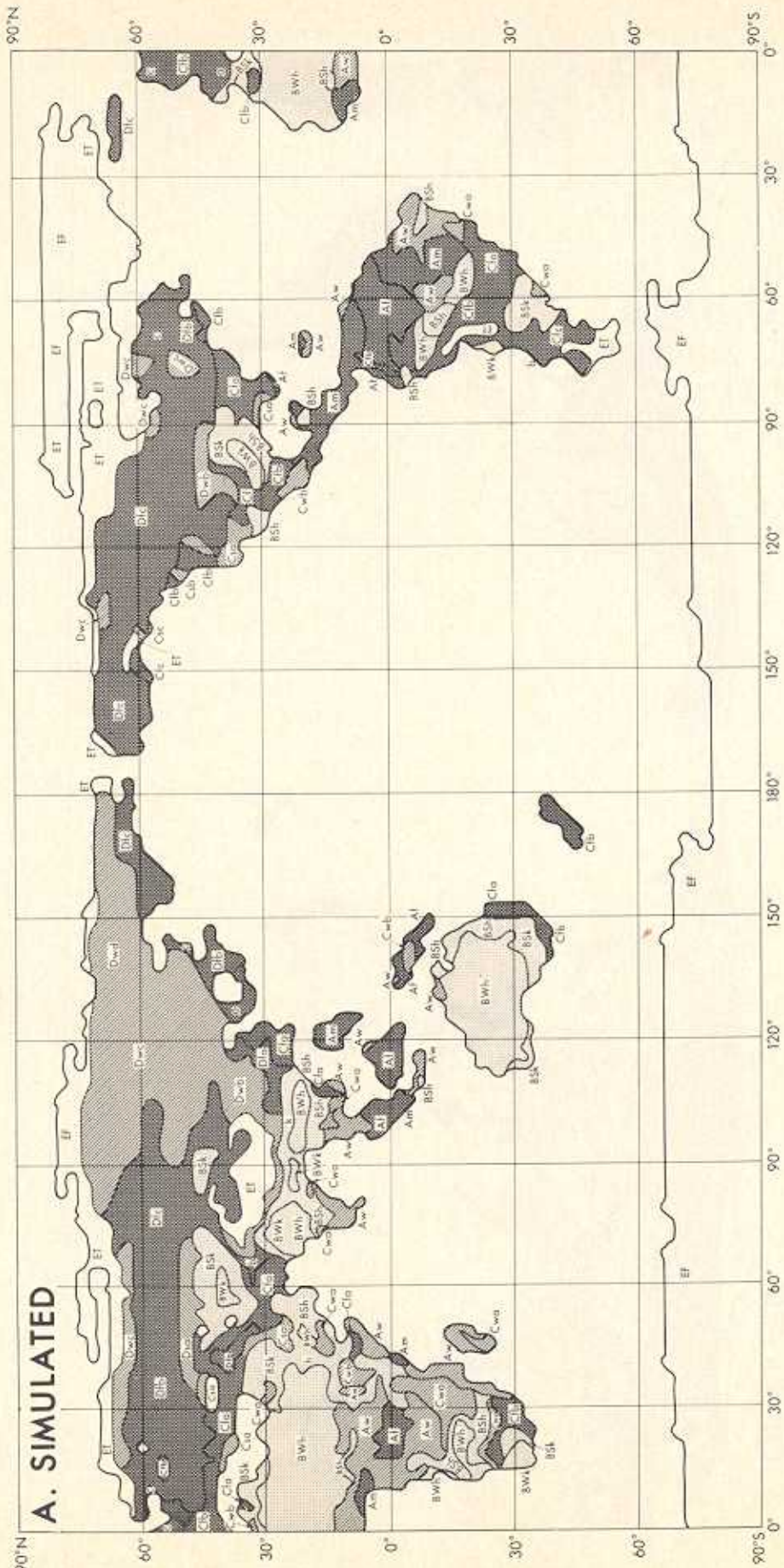

Fig. 32 (*a*). Global distribution of Köppen climate types based on model-simulated data.

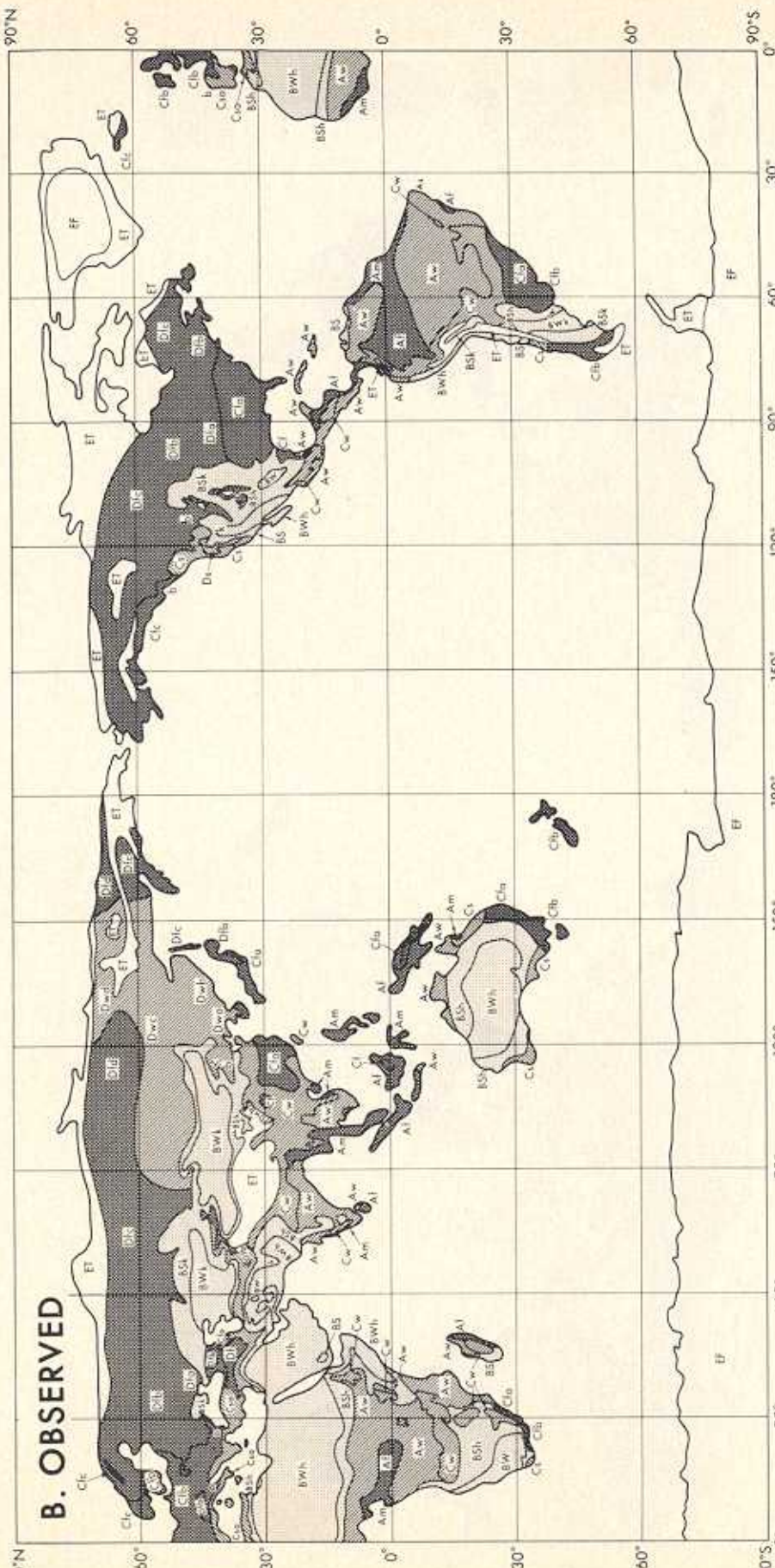

Fig. 32(*b*). Global distribution of Köppen climate types based on observed data [*Trewartha*, 1968].

winter. Accordingly, a significant amount of rainfall occurs in this no-mountain model in the otherwise arid region of middle latitudes. *Hahn and Manabe* [1975] have shown that the south Asian low is shifted to the northeastern part of China in a mountainless model in July. Again the rate of precipitation over central Asia is significantly enhanced as a result of the removal of mountains. In short, it may be necessary to take into consideration the effects of mountains to explain the existence of the arid region in central Asia.

One of the unrealistic features of the model climate is that the B climate in the northwestern part of India extends incorrectly through the plain region of India into south China, where a Cw climate ought to prevail instead. These discrepancies result from the unrealistically meager precipitation in these regions during summer, as mentioned earlier. The BW climate in the southeastern part of China results from the excessive development of tropical cyclones in the western Pacific which prevent the maritime air from entering the continent [*Manabe et al.*, 1974]. The arid regions in southern Africa and southern South America are approximately correctly positioned by the model, although their areal extent is somewhat less than occurs on the earth. The excessively dry belt simulated along the southwestern border of Brazil may have resulted from penetration of the subtropical dry area of the southeastern Pacific Ocean through the gap in the Andes Mountains at 5°S into the central part of the continent. This unrealistic gap in this mountain range is created by the smoothing necessary in the model's topography (Figure 1). The arid region in the southwestern part of North America is not realistically located in the model. It is shifted from its true location in western United States to the southern part of the country. This error is consistent with deficiencies in the model simulation of precipitation in southern United States, mentioned earlier.

The area of Cf climate over the southeastern part of North America is significantly wider than that over the Eurasian continent (eastern part of China), in qualitative agreement with features of the observed climate in these areas. This difference stems from the orographic differences between the two continents. Over the Eurasian continent an intense Siberian high prevails during winter because of the effects of the Himalayas [*Mintz*, 1965; *Manabe and Terpstra*, 1974]. Very cold and dry northerly winds along the eastern periphery of this anticyclone bring a dry winter to the east coast of Asia. On the other hand, such an intense high does not develop over North America in winter. Instead, a weaker high develops in the southwestern part of this continent. Humid air often penetrates into the eastern half of the United States and accounts for the moderate wetness of the Cf climate there in winter.

Generally, on the western sides of continents, poleward from the subtropical arid regions (BW and BS climates), rainfall is moderate but is confined to the winter half of the year because in summer the subtropical high-pressure belt approaches these regions more closely. Therefore in these areas, Cs climates prevail. Examples of these areas are the Pacific coast of the United States and along most of the Mediterranean coast. The model simulates many of these areas of Cs climate in western United States and Canada but fails to recognize the summer dry areas of most of the Mediterranean coast.

The colder wet temperate climates (Df and Dw) are reasonably well located by the model simulation except in Mongolia and in the Rocky Mountain region of North America, where the computed climate is in many places D type rather than arid. The extensive area of Dw climate in eastern Siberia results from very cold dry winters produced there by the dry northerly winds around the strong Asian anticyclone at this season. (A discussion of the mean winter pressure distribution is presented in an earlier section.) On the other hand, a Dw climate fails to occur in Canada because high pressure does not dominate North America during winter as it does in east Asia. The model erroneously specified a few Dw areas in the United States and Canada, but in general it simulates the predominance of Df climate on the northern half of this continent.

The temperature subtypes of the C and D climates are well delineated by the model. For example, there is a gradual transition from the Dfa climate in European Russia to the coldest D climate (Dfd) as one advances northeastward into northern Siberia. This is simulated well in the model except for w or s replacing f in some areas in the model. This pattern of climates is consistent with the decrease in temperature from west to east in the northern Eurasian continent noticed in Figure 6.

Finally, the model simulates the locations of polar climates rather accurately. For example, the model correctly specified a tundra (ET) climate along the northern fringes of Canada and Siberia and even at the southern tip of South America. In addition, the model properly reproduces the perpetual frost (EF) climate of central Greenland and Antarctica. The model simulation also correctly locates tundra climates resulting from high altitude (ET) on the Tibetan Plateau and in the Andes Mountains of South America.

The Köppen climatic types derived in this paper are based on means for only 1 model simulation year. Somewhat different values of temperature and precipitation means could be expected if more than 1 model year were used because the model is probably subject to year-to-year variations. In fact, the means of hydrologic quantities obtained from the previous year's simulation exhibit some significant differences from the last year of the model experiment analyzed in this paper. However, the first year of the time integration is probably less representative of the model climate because of the adjustment to the doubling of grid network resolution immediately before the beginning of that model year. On the other hand, extending the time integration to obtain more stable climatic averages would have been very expensive.

SUMMARY AND CONCLUSIONS

The global model of the atmosphere described here is capable of simulating major features of the seasonal variations of the tropospheric climate and of the hydrologic cycle. The distribution of Köppen climatic types, based on simulated temperatures and precipitation rates throughout the model year, agrees well with that derived from observed data, in both delineating wet and arid zones of the earth and in representing the temperature distribution over the continents.

The mean sea level pressure patterns created by the model exhibit Aleutian and Icelandic lows in roughly the proper locations, though the intensity of the Aleutian low is exaggerated. The model simulates a strong Siberian high over Asia in winter, which is replaced by a south Asian low in summer. This seasonal reversal of pressure patterns in Asia accounts for the model's realistic winter-to-summer shift in the simulated monsoon circulation over this continent. Over North America the model correctly reproduces the winter anticyclone and summer cyclone in the southwestern part of the continent. These pressure systems are much weaker and less extensive than those over the Eurasian continent. It is

suggested that this intercontinental difference results partly from the influence of the longitudinal barrier over the Eurasian continent, i.e., the Tibetan Plateau. In the southern hemisphere the model approximately simulates the intensities and the locations of subtropical highs, particularly in the summer season. However, it fails to simulate the belt of deep low pressure along the periphery of the Antarctic continent. It is speculated that this difficulty may result from the failure of the model to incorporate the effects of the steep Antarctic mountains properly.

The seasonal variation of the precipitation rate is well simulated by the model. For example, the tropical rain belt of the model shifts with respect to season in a manner similar to the movement of the actual rain belt. Over oceanic regions it tends to develop in areas of relatively warm sea surface temperature, whereas on land it migrates over a wide range of latitudes with change in season. This migration accounts for the transition from a dry winter to a wet summer, which takes place at both sides of the model equator (i.e., in regions of savanna climate). The rates of rainfall near the model equator are greater over continents than over oceans partly because of the suppression of tropical disturbances and rainfall above the belt of cold surface water at the model equator. Unfortunately, the rate of precipitation in the continental region of the model tropics is much larger than the observed rate which results in excessive runoff. The cause for this difficulty has not been identified.

The model simulates minimums of precipitation in the subtropics where the downward-moving branch of a Hadley cell is located. Accordingly, the areas of low values of simulated soil moisture correspond to the major deserts of the world, such as the Sahara of north Africa, the Thar Desert in northwestern India, the Arabian Desert, and the deserts in Australia and southwest Africa. There are, however, some significant differences between the computed distribution of arid regions and the actual. For example, the model produces a desert in the southeastern part of China. Over North America the Great Western Desert extends too far eastward and covers Texas.

In middle latitudes of the model the rate of precipitation on land is greatest in summer, whereas over oceans it is at a maximum in winter. This result is consistent with the seasonal variation of surface pressure mentioned earlier in this section. Over the Eurasian continent of the model, subsiding northerlies blow along the periphery of the intense Siberian high during winter in a manner similar to the actual outbreak of cold air in this region. Accordingly, the rate of precipitation is very low along the east coast of the continent. On the other hand, the computed rate of precipitation is not as small on the east coast of North America during winter, in agreement with the features of the actual precipitation. As mentioned already, the Siberian high extends farther eastward than the subtropical high over North America and is responsible for this difference. The arid region corresponding to the Gobi Desert is correctly located in the model at relatively high latitudes, though it is much less extensive than the real Gobi Desert. Based upon the results from the present simulation study and those of other numerical experiments, it is suggested that the Tibetan Plateau is responsible for the maintenance of deserts extending from Turkestan to the Gobi Desert in middle latitudes.

In the subarctic region of the model, such as northern Europe, Siberia, and Canada, the precipitation rate is not very large, but a humid climate and wet soil are maintained there because of insufficient insolation to deplete the scarce moisture by evaporation. In eastern Siberia, however, precipitation tends to be low during winter, owing to the strong northwesterlies blowing along the periphery of the Siberian high. These features of the model are in excellent qualitative agreement with those of the actual climate.

The global distribution of runoff of the model compares qualitatively with estimates of actual runoff contained in the *Mira Atlas* [1965]. It is noteworthy that the regions in the model having high rates of runoff correspond to the watersheds of the major rivers in the world, i.e., the Amazon River, the Congo River, and the rivers in the subarctic region, such as the Mackenzie River in Canada and many large rivers in Siberia. A major source of water for these subarctic rivers is snowmelt in late spring. As pointed out already, the runoff in tropical rivers is too large. On the other hand, some of the watersheds of the model are dryer than on the real earth. For example, the Mississippi River basin in central United States and the Yangtze River basin in the southern part of China have low rates of runoff due to the deficiency in the simulated precipitation rates in these areas.

In general, the model tends to perform poorly in the neighborhood of major mountain ranges. As previously mentioned, the low-pressure belt along the periphery of the Antarctic continent is too weak in the model simulation. The computed rate of precipitation in northern India during the period of the southern Asian summer monsoon is significantly less than the actual rate, which is probably due to the failure of the model to deal with the steep southern slope of the Himalayas [*Hahn and Manabe*, 1975]. Over South America in the model the simulation is relatively poor partly because of the difficulty in coping with the steep Andes mountain range. As already pointed out in this section, the location of the Great Western Desert to the west of the Rockies is not simulated properly. In view of the difficulties listed above it is necessary to improve the technique for treating the flow over and around steep mountains.

In conclusion, it is encouraging that the model described in this study is capable of simulating the gross features of the global distribution of various hydrologic quantities despite the extreme simplifications of the hydrologic processes incorporated in the model. Therefore we feel that the model is realistic enough for carrying out many sets of numerical experiments to identify the factors which control the hydrologic cycle and climate. For example, the model may be used to study how major mountain ranges affect climate or how anomalies in sea surface temperature alter the distribution of precipitation rate. In addition, one can study how the distribution of soil moisture and runoff depend upon key parameters such as field capacity of soil and the albedo of the earth's surface. Sensitivity studies of this sort are indispensable in determining the strategy for further improvements of the parameterization of hydrologic processes.

Acknowledgments. The authors are very much indebted to J. Smagorinsky, who has provided much valuable advice and wholehearted support throughout the course of this work. We gratefully acknowledge the many useful suggestions given by Y. Kurihara for improving the model and enabling us to carry out a successful time integration. D. Hahn is sincerely thanked for writing the diagnostic computer programs and for performing the statistical analysis of the simulated model results. We greatly appreciate the very careful review of the manuscript made by J. D. Mahlman. We wish to thank D. Daniel for his effective day-by-day management of the model's time integration on the computer. Finally, we are very grateful to L. Dimmick, P. Tunison, and E. Green and E. Groch and M. Callan, whose assistance was indispensable in the preparation of the figures and the manuscript.

REFERENCES

Baumgartner, A., and E. Reichel, Eine neue Bilanz des globalen Wasserkreislaufes, *Umschau, 20*, 631–632, 1973.

Bjerknes, J., L. J. Allison, E. R. Kreins, F. A. Godshall, and G. Warnecke, Satellite mapping of the Pacific tropical cloudiness, *Bull. Amer. Meteorol. Soc., 50*, 313–322, 1969.

Budyko, M. I., *The Heat Balance of the Earth's Surface* (in Russian), Gidrometeorologicheskoe Izdatel'stvo, Leningrad, 1956. (Translated from Russian by N. A. Stepanova, Office of Technical Services, U.S. Department of Commerce, Washington, D. C., 1958.)

Budyko, M. I., *Atlas of the Heat Balance of the Earth*, (in Russian), USSR Glavnaia Geofizicheskaia Observatoriia, Moscow, 1963.

Budyko, M. I., The water balance of the ocean, Proceedings of Symposium on World Water Balance, Reading, England, vol. 1, *Publ. 92*, pp. 24–33, Int. Ass. of Sci. Hydrol. and U.N. Educ., Sci., and Cult. Organ., Gentbrugge, Belgium, 1970.

Crutcher, H. L., and J. M. Meserve, Selected level heights, temperatures and dew points for the northern hemisphere, *NAVAIR 50-1C-52*, 8 pp. and charts, U.S. Nav. Weather Serv. Command, Washington, D. C., 1970.

Hahn, D. G., and S. Manabe, The role of mountains in the south Asian monsoon circulation: A comparison of two global general circulation model experiments, Geophys. Fluid. Dyn. Lab./NOAA, Princeton, N. J., to be published, 1975.

Haurwitz, B., and J. M. Austin, *Climatology*, McGraw-Hill, New York, 1944.

Hering, W. S., and T. R. Borden, Jr., Mean distributions of ozone density over North America 1963–1964, *Environ. Res. Pap. 162*, 19 pp., U.S. Air Force Cambridge Res. Lab., Hanscom Field, Bedford, Mass., 1965.

Holloway, J. L., Jr., and S. Manabe, Simulation of climate by a global general circulation model, *Mon. Weather Rev., 99*, 335–370, 1971.

Holloway, J. L., Jr., and S. Manabe, Numerical simulation of the seasonal variation of the atmospheric hydrologic cycle, Proceedings of the 1974 Summer Computer Simulation Conference, pp. 246–249, Amer. Inst. of Chem. Eng. et al., New York, 1974.

Holloway, J. L., Jr., M. J. Spelman, and S. Manabe, Latitude-longitude grid suitable for numerical time integration of a global atmosphere model, *Mon. Weather Rev., 101*, 69–78, 1973.

Kasahara, A., and W. M. Washington, General circulation experiments with a six-layer NCAR model, including orography, cloudiness and surface temperature calculations, *J. Atmos. Sci., 28*, 657–701, 1971.

Köppen, W., *Grundriss der Klimakunde*, Walter de Gruyter, Berlin, 1931.

Kurihara, Y., and J. L. Holloway, Jr., Numerical integration of a nine-level global primitive equations model formulated by the box method, *Mon. Weather Rev., 95*, 509–530, 1967.

Leith, C. E., Numerical simulation of the earth's atmosphere, in *Methods in Computational Physics*, vol. 4, *Applications in Hydrodynamics*, edited by B. Alder, S. Sernback, and M. Rotenberg, pp. 1–28, Academic, New York, 1965.

Lvovitch, M. I., and S. P. Ovtchinnikov, *Physical-Geographical Atlas of the World* (in Russian), Academy of Sciences, USSR, and Department of Geodesy and Cartography, State Geodetic Commission, Moscow, 1964.

Manabe, S., Climate and the ocean circulation, 1, The atmospheric circulation and the hydrology of the earth's surface, *Mon. Weather Rev., 97*, 739–774, 1969.

Manabe, S., and J. L. Holloway, Jr., Climate modification and a mathematical model of atmospheric circulation, in *A Century of Weather Progress*, edited by J. E. Caskey, Jr., pp. 157–164, American Meteorological Society, Boston, Mass., 1970.

Manabe, S., and R. F. Strickler, Thermal equilibrium of the atmosphere with a convective adjustment, *J. Atmos. Sci., 21*, 361–385, 1964.

Manabe, S., and T. B. Terpstra, The effects of mountains on the general circulation of the atmosphere as identified by numerical experiments, *J. Atmos. Sci., 31*, 3–42, 1974.

Manabe, S., and R. T. Wetherald, Thermal equilibrium of the atmosphere with a given distribution of relative humidity, *J. Atmos. Sci., 24*, 241–259, 1967.

Manabe, S., J. Smagorinsky, and R. F. Strickler, Simulated climatology of a general circulation model with a hydrologic cycle, *Mon. Weather Rev., 93*, 769–798, 1965.

Manabe, S., J. L. Holloway, Jr., and H. M. Stone, Tropical circulation in a time-integration of a global model of the atmosphere, *J. Atmos. Sci., 27*, 580–613, 1970.

Manabe, S., J. L. Holloway, Jr., and D. G. Hahn, Seasonal variation of climate in a time-integration of a mathematical model of the atmosphere, paper presented at Symposium of Physical and Dynamical Climatology, World Meteorol. Organ., Leningrad, August 16–20, 1971.

Manabe, S., D. G. Hahn, and J. L. Holloway, Jr., The seasonal variation of the tropical circulation as simulated by a global model of the atmosphere, *J. Atmos. Sci., 31*, 43–83, 1974.

Mastenbrook, H. J., The vertical distribution of water vapor over Kwajalein Atoll, Marshall Islands, *NRL Rep. 6367*, 11 pp., U.S. Nav. Res. Lab., Washington, D. C., Dec. 30, 1965.

Mather, J. R., The average annual water balance of the world, AWRA Symposium Proceedings, Amer. Water Res. Ass., Chicago, Ill., 1970.

Mintz, Y., Very long-term global integration of the primitive equations of atmospheric motion, Proceedings of WMO-IUGG Symposium on Research and Development Aspects of Long-Range Forecasting, *WMO Tech. Note 66*, pp. 141–167, World Meteorol. Organ., Geneva, 1965.

Mira Atlas, *Physical-Geographical Atlas of the World* (in Russian), Academy of Sciences, USSR, and Department of Geodesy and Cartography, State Geodetic Commission, Moscow, 1964. (Review and English translation, vol. 6 (5–6), American Geographical Society, New York, 1965).

Möller, F., Quarterly charts of rainfall for the whole earth (in German), *Petermanns Geograph. Mitt., 95*, 1–7, 1951.

Neumann, G., and W. J. Pierson, Jr., *Principles of Physical Oceanography*, pp. 76–78, Prentice-Hall, Englewood Cliffs, N. J., 1966.

Oort, A. H., and E. M. Rasmusson, On the annual variation of the monthly mean meridional circulation, *Mon. Weather Rev., 98*, 423–442, 1970.

Oort, A. H., and E. M. Rasmusson, Atmospheric circulation statistics, *NOAA Prof. Pap. 5*, 323 pp., U.S. Govt. Print. Office, Washington, D. C., 1971.

Phillips, N. A., Energy transformation and meridional circulations associated with simple baroclinic waves in a two-level, quasi-geostrophic model, *Tellus, 6*, 273–286, 1954.

Phillips, N. A., A coordinate system having some special advantages for numerical forecasting, *J. Meteorol., 14*, 184–185, 1957.

Smagorinsky, J., General circulation experiments with primitive equations, 1, The basic experiment, *Mon. Weather Rev., 91*, 99–164, 1963.

Taljaard, J. J., H. van Loon, H. L. Crutcher, and R. L. Jenne, Climate of the upper air, 1, Southern hemisphere, vol. 1, Temperatures, dew points, and heights at selected pressure levels, *NAVAIR 50-1C-55*, 135 pp., U.S. Nav. Weather Serv., Washington, D. C., 1969.

Trewartha, G. T., *An Introduction to Climate*, 4th ed., McGraw-Hill, New York, 1968.

U.S. Navy Hydrographic Office, World atlas of sea surface temperature, 2nd ed., *Publ. 225*, with suppl., Washington, D. C., 1964.

Washington, W. M., On the role of radiation in dynamical climate simulation and numerical weather prediction, Proceedings of Miami Workshop on Remote Sensing, pp. 39–67, NOAA, Boulder, Colo., 1971.

Washington, W. M., and A. Kasahara, A January simulation experiment with the two-layer version of the NCAR global circulation model, *Mon. Weather Rev., 98*, 559–580, 1970.

(Received August 22, 1974;
accepted December 20, 1974.)